Correlation of Diffusion Tensor Imaging Indices with Histological Parameters in Rat Cervical Spinal Cord Gray Matter Following Distal Contusion Spinal Cord Injury

Robin Easow Mottackel
Marquette University

CORRELATION OF DIFFUSION TENSOR IMAGING INDICES WITH HISTOLOGICAL PARAMETERS IN RAT CERVICAL SPINAL CORD GRAY MATTER FOLLOWING DISTAL CONTUSION SPINAL CORD INJURY

By

Robin E. Mottackel, B.E.

A Thesis submitted to the Faculty of the Graduate School,
Marquette University,
in Partial Fulfillment of the Requirements for the
Degree of Master of Science

Milwaukee, Wisconsin

December 2010

ABSTRACT

CORRELATION OF DIFFUSION TENSOR IMAGING
INDICES WITH HISTOLOGICAL PARAMETERS IN
RAT CERVICAL SPINAL CORD GRAY MATTER
FOLLOWING DISTAL CONTUSION
SPINAL CORD INJURY

Robin E. Mottackel, B.E.

Marquette University, 2010

The purpose of this study was to delineate the diffusion tensor imaging (DTI) parameters across the cervical spinal cord gray matter (GM) in a distal (T8) rat contusion spinal cord injury (SCI) model. DTI data were obtained from ex vivo rat spinal cords and registered to corresponding histological slices in samples from the acute through chronic stages of SCI including uninjured control, 2 weeks post injury, 15 weeks post injury and 25 weeks post injury groups (n = 5 in all groups). After imaging, samples were dehydrated, blocked in paraffin, sliced axially and stained with eriochrome cyanine R stain and H&E counter-stain. A corresponding sample was post fixed with osmium tetroxide and stained with toluidine blue. Histology images of the eriochrome cyanine R stained and H&E counter-stained slices were captured at 4x and then segmented into white matter (WM) and GM and dorsal and ventral GM using a custom cluster analysis. Using whole cord templates, DTI images for each animal were then registered to the corresponding histology images. The WM and the GM regions of interest (ROI) histological templates were then used to map DTI indices, including fractional anisotropy (FA), longitudinal apparent diffusion coefficient (lADC) and transverse apparent diffusion coefficient (tADC) across the GM. The average values for each index were also calculated in predefined gray matter ROIs. Histology images of the above mentioned ROIs were captured at 40x resolution using the toluidine blue stained slices for the control and post injury groups (n=4). Motoneuron size in the ventral GM was calculated for each of the control and post injury groups. It was observed that the FA and lADC values in the dorsal GM ROI were significantly higher than that in the ventral GM ROI in controls, fifteen weeks post injury and twenty five weeks post injury groups ($P < 0.05$). The overall GM FA value at twenty five weeks was significantly higher than the FA value at two weeks post injury ($P < 0.05$) and the FA value in controls ($P < 0.05$). Group analysis of the size of the motor neurons showed a 9% increase in the motoneuron size at two weeks ($P < 0.01$) and 42% increase at twenty five weeks ($P < 0.01$) post injury as compared to controls. The motor neurons also showed a significant increase in size at twenty five weeks post injury ($P < 0.01$) as compared to the motor neuron size at two weeks post injury. These results indicate changes in gray matter structure rostral to a contusion injury that can be detected and monitored using DTI.

ACKNOWLEDGEMENTS

Robin E. Mottackel, B.E.

But those who hope in the Lord
will renew their strength.
They will soar on wings like eagles;
they will run and not grow weary,
they will walk and not be faint.
-Isaiah 40:31

I would like to dedicate this thesis to my personal savior, Jesus Christ, and my parents Mr. Easow Thomas and Mrs. Leela Thomas. I would like to thank my sisters Ms. Roselin Easow, Ms. Roshni Easow and Ms. Ruby Easow for their continued support.

I would like to thank the members of my committee for their support in this research. I would like to thank my mentor and advisor Dr. Brian D. Schmit for his guidance and support. I am deeply indebted to my thesis committee members Dr. Taly Gilat-Schmidt and Dr. Shekar Kurpad for their expert assistance in this multifaceted project. I would also like to thank Dr. Benjamin Ellingson for his support and assistance in analyzing the DTI data.

I would also like to thank Mr. Renji Thomas, Mr. Ryan McKindles and Mr. Benjamin Kalinosky and Ms. Jain Mangalathu for the productive brainstorming sessions I had with them. I would also like to thank all the members of the Neuromechanics Laboratory as well as the faculty of the biomedical engineering department at Marquette University.

TABLE OF CONTENTS

LIST OF TABLES

LIST OF FIGURES

Chapter 1:

Introduction

The phenomenon of diffusion was first elucidated by Robert Brown in 1827 and Albert Einstein in 1905 in their seminal findings (Brown 1828; Einstein 1905). The aim of this thesis, in its most basic form, was to utilize precise and non-invasive imaging techniques to gauge, quantify and analyze diffusion behavior in living tissue. This would ultimately lead to clarity in the understanding of tissue diffusion properties in health as well as sickness. In order to achieve the aforementioned aim, this thesis uses diffusion weighted imaging (DWI) and diffusion tensor imaging (DTI) which are robust, non-invasive imaging techniques based fundamentally on the phenomenon of diffusion. In order to understand the principles of DWI and DTI, a firm understanding of the concept of diffusion is a prerequisite. To better visualize diffusion, consider the example of a glass of water. To the naked eye, the water in the glass appears stationary. However, at a microscopic level, every molecule is in random motion. This random motion is manifested to the naked eye when we place a drop of ink in the glass of water. The two liquids merge together to form a homogeneous distribution of murky liquid, never to return to its initial state spontaneously. Since diffusion basically constitutes motion of water molecules, it can be used as a probe to investigate the physical properties, integrity, shape, permeability and three dimensional arrangements of barriers to molecular displacement. Based on this, DWI and its successor DTI can be used to understand the diffusion properties in a biological system (Moseley, Kucharczyk et al. 1990; Moseley, Kucharczyk et al. 1991; Beaulieu 2002).

DWI and DTI fundamentally have their roots in Magnetic resonance imaging (MRI), a medical imaging modality that has gained wide spread use as a flexible and robust imaging technique to gain insight into the human body. This is due to the many

advantages MRI has over other imaging modalities, namely its non-invasive nature and the absence of any adverse effects. For example, positron emission tomography (PET) and computed tomography (CT) are excellent imaging modalities in their own right but both suffer from the harmful effects of ionizing radiation. The signal acquired in MRI is affected by a myriad of physical, chemical and biological properties, resulting in excellent contrast mechanisms that provide an exceptional understanding of bio-systems and help in diagnosis and prognosis of disease.

Although MRI is an excellent imaging modality, it displays shortcomings when used to image the spinal cord. Traditional MRI sequences, based on proton density weighted by longitudinal and transverse relaxation times, fail to provide adequate sensitivity to the structure of the spinal cord following spinal cord injury (SCI). It has been shown that gross morphological or MR imaging abnormalities of the spinal cord can be absent during the immediate phase following SCI with the exception of patients suffering from severe compressive or lacerative injuries (Aoyama, Hida et al. 2007). This calls for an imaging technique which is more sensitive to the underlying spinal cord microstructure than traditional MRI.

Diffusion weighted imaging (DWI) overcomes this shortcoming of MRI. DWI is an MRI technique that measures the attenuation of the MR signal due to incoherent motion of unbound water molecules(Basser and Jones 2002). The diffusion of water molecules is appealing because water molecules are abundant in living tissue and are harmless. This, coupled along with the ability of diffusing water molecules to probe surrounding tissue microstructure is the main motivation and principle behind DWI. Indeed, diffusion DWI and DTI have shown significant sensitivity to structural changes

within the human spinal cord following acute spinal trauma and chronic spinal cord injury (Sagiuchi, Tachibana et al. 2002; Ellingson, Ulmer et al. 2006).

This thesis is motivated by a strong appreciation of the advantages of DWI and DTI mentioned above and a firm understanding of the current status of research in SCI using DWI and DTI. DTI has been used extensively to study specific axonal tracts in the spinal cord white matter following spinal cord injury (Kim, Loy et al. ; Ellingson, Ulmer et al. 2006; Kozlowski, Raj et al. 2008; Zhang, Jones et al. 2009); however, there is a lack of clarity with regards to diffusion parameters in the spinal cord gray matter following spinal cord injury. To date there have been no studies correlating spinal cord gray matter cytoarchitecture to the DTI indices following spinal cord injury. Also, a firm understanding of the correlation between DTI characteristics in the cervical spinal cord gray matter and the underlying gray matter neuronal structure is yet to be established. In addition to this, most DTI studies done until now have used one of the following methods to select ROIs. They are either based on user selected ROI's or on segmentation based on atlas templates since segmentation techniques are not robust enough to segment white matter and gray matter in the DTI indices automatically because of the relatively low resolution of spinal cord imaging. Segmentation based on manual user-selected ROIs could suffer from human error and does not include the entire region, but rather incorporates a sample area in the region of interest. Along with this, segmentation based on generic atlas templates suffer from error in registration due to inter-subject variability.

Based on this background, this research tries to address the limitations and fill gaps in the current state of research in SCI using DTI. This thesis tries to further the understanding of diffusion in the spinal cord gray matter in health and injury using DTI.

Firstly, this thesis develops an automatic technique to segment ROIs in the gray matter of the rat spinal cord in DTI contrast images. Secondly, this technique is applied to quantify and characterize the spatio-temporal diffusion characteristics of the rat cervical spinal cord gray matter. Finally, these diffusion characteristics are correlated with underlying gray matter neuronal structure using histology.

This thesis is organized as follows. Chapter 1 provides the appropriate framework for this research and lists the fundamental issues that inspired this thesis. Chapter 2 discusses the basics of MRI, DWI and DTI. This is followed by a review of the normal gross anatomy and physiology of the spinal cord. The pathology, mechanism and time course of inflammatory response in the spinal cord following spinal cord injury is also discussed in this chapter. This is followed by a review of the spinal cord diffusion characteristics using DTI in health and injury as reported by previous studies. This chapter finally winds up explaining the mathematical principles behind the image processing techniques used in this particular thesis. Chapter 3 presents the study correlating diffusion tensor imaging indices with histological parameters in rat cervical spinal cord gray matter following distal contusion spinal cord injury.

Chapter 2:

Background

2.1 Magnetic Resonance Imaging

Magnetic resonance imaging (MRI) is one of the two major fields that constitute nuclear magnetic resonance (NMR), the other being magnetic resonance spectroscopy (MRS). MRS is widely used in the field of chemistry to analyze the composition of a wide range of compounds while MRI is widely used in the medical field as an imaging tool. This wide scale use of MRI as a clinical diagnosis tool led to the deletion of the term "nuclear" from NMR to prevent the idea that MRI is related to either radioactivity or nuclear medicine techniques.

Although MRI is a relatively new technique, the foundations for MRI were first laid in the 1940s.The physical phenomenon of NMR was first discovered independently by Bloch (Bloch, Hansen et al. 1946) and Purcell (Purcell, Torrey et al. 1946) in the year 1946 for which they received the Noble Prize in Physics in 1952. The basis for the use of NMR to analyze chemicals was established by Proctor (Proctor and Yu 1950) and Dickinson (Dickinson 1950) in their pioneering work in 1950. Both independently found chemical shift effects in the NMR spectra. Damadian, in his original work, showed the possibility of using NMR for medical diagnosis by studying the differences in relaxation times between different tissues and between normal and cancerous tissues (Damadian 1971). More recently the ground breaking work of Lauterbur (Lauterbur 1973) and Mansfield (Mansfield 1977) led to vast improvements in the field of MRI which led to them being awarded the Noble Prize in 2003. Lauterbur's work had profound effect on the development of MRI, as he proposed the use of a gradient of the main magnetic field to enforce a linear variation of the frequency of MR signals as a function of the spatial

location of their source. Mansfield introduced the echo planar technique providing the basis for fast imaging speeds. Since these studies were published, the field of MRI has been growing at a remarkable rate with respect to its use a medical imaging tool.

2.1.1 Principles of MRI

The fundamental physical property of spin, which is possessed by every elementary particle, is the foundation for MRI. Nucleons have spin which can pair up when the orbital are being filled and cancel out. More or less every element in the periodic table has an isotope possessing a non zero nuclear spin. The nucleus with a non zero spin possesses a magnetic moment, analogous to that of the magnetic bar in which the magnetic field is oriented from the south to the north pole, as shown in *Figure 2.1*. In the absence of an external magnetic field, the magnetic moments of the nuclear spins will have random orientation, so the net effect of these nuclear spins will be zero, as show in *Figure 2.2*.

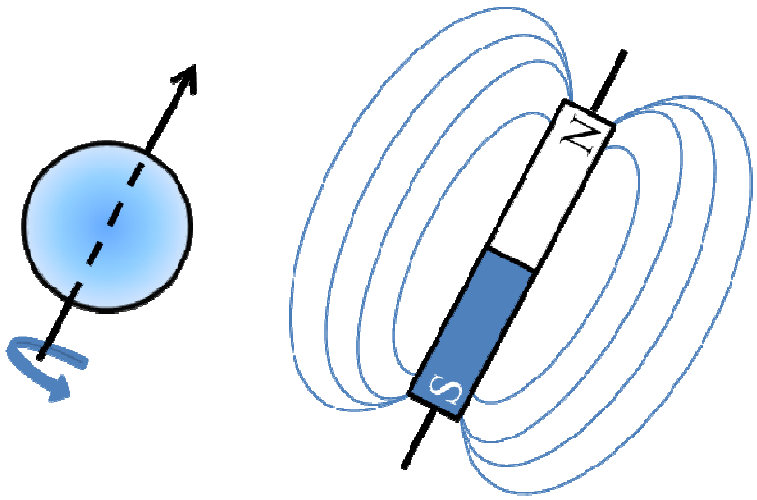

Figure 2.1: Analogy of a rotating spin to the magnetic field produced by a magnetic bar.

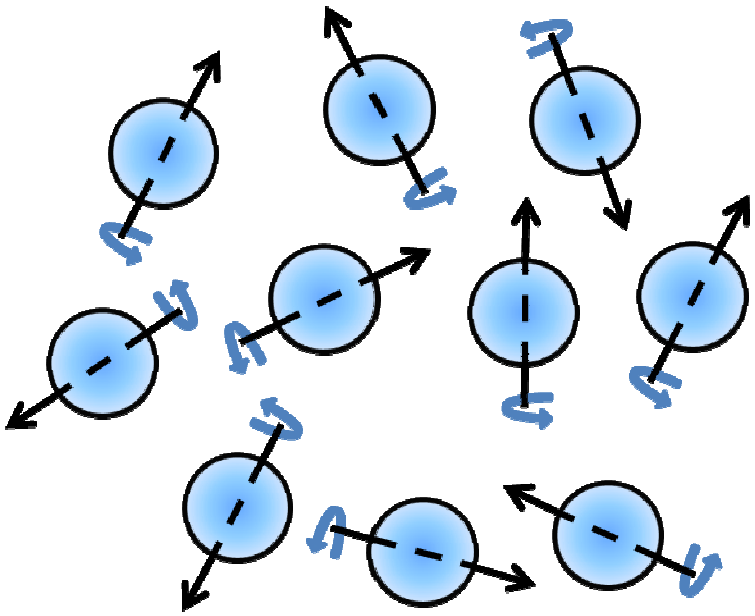

Figure 2.2: Random orientation of the magnetic moments of the nuclear spins in the absence of an external magnetic field.

In order for a nucleus to be manipulated using an external magnetic field, it has to have a non-zero nuclear spin and has to be naturally present in abundance so that it can be detected using MRI. Some of the nuclei that are of interest in MRI are listed in Table 2.1. For clinical MRI, the hydrogen nuclei (^1H) is the most commonly used nuclei as it gives the strongest signal and is most abundant in the human body.

Nucleus	Atomic number	Gyromagnetic ratio (Mhz/Tesla)
Hydrogen	1	42.58
Carbon	13	10.71
Nitrogen	15	4.31
Oxygen	17	5.77
Fluorine	19	40.05
Sodium	23	11.26
Phosphorus	31	17.23

Table 2.1: Nuclei of interest in MRI.

When an external magnetic field (B_0) is applied, the nuclear spins align parallel or anti-parallel to the external magnetic field (*Figure 2.3A*). The parallel state of the nuclear spin is the low energy state while the anti-parallel state of the nuclear spin is the high energy state. There is a slight excess of the parallel nuclei compared to the anti-parallel nuclei leading to a net magnetization (*M*) in the direction of the external field B_0 at the equilibrium stage (*Figure 2.3B*). The parallel and the anti parallel nuclei also precess around the fixed axis of the external magnetic field B_0 (*Figure 2.3B*) with a frequency called the Larmor frequency which is defined by equation (*2-1*).

$$w_o = \lambda B_0 \tag{2-1}$$

In this equation, w_o is the frequency of the precession, B_0 is the magnetic field strength and λ is gyromagnetic ratio which is a property of the different nuclei. For hydrogen (^1H), λ is approximately 42.58MHz/T.

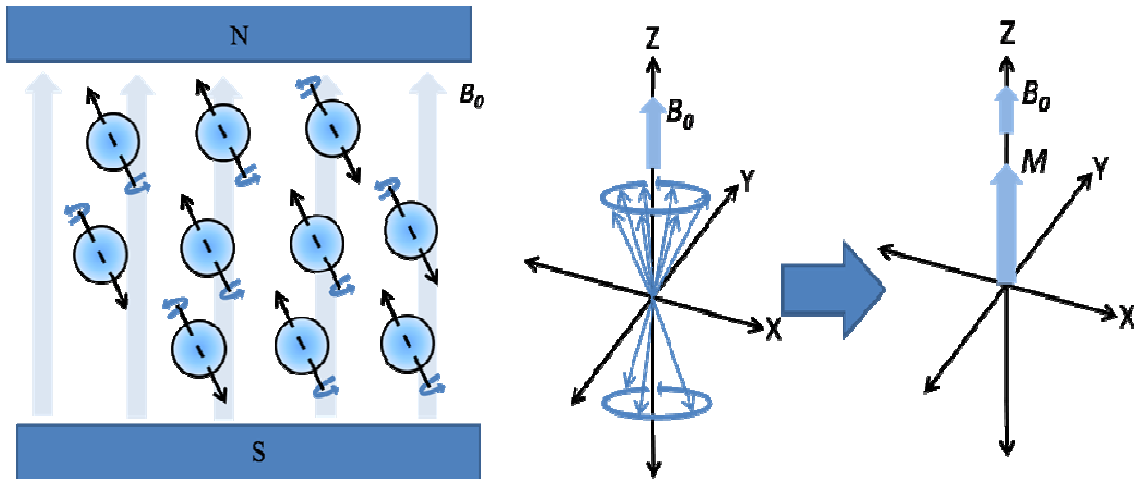

A **B**

Figure 2.3: A) Nuclear spins aligned parallel and anti parallel to the external magnetic field B_0. B) Nuclei in both the parallel and the anti parallel states precessing around the axis of the external magnetic field B_0 leading to a net magnetization (M) in the direction of the external field B_0.

To measure the magnetic resonance (MR) signal, the spins in equilibrium state must be excited by a radio frequency (RF) pulse. The RF pulse is tuned in such a way that its frequency is equal to the Larmor frequency. This RF pulse is then applied along the transverse (X-Y) plane. The RF pulse is also called the B_1 field. When the B_1 field is applied the energy is absorbed by ^1H nuclei, after which the distribution of the parallel and anti-parallel states is disturbed and the phase of the spins is aligned. Due to realignment of spins, the longitudinal magnetization *M* is flipped down a certain angle from the z-direction. This angle of flip is determined by the strength of the B_1 field and its duration. A 90 degree RF pulse is mostly used in MR signal measurement which tips the vector *M* into the X-Y plane (*Figure 2.4*). The flip angle is defined by the equation (*2-2*)

B_1 (2-2)

In this equation, is the flip angle, λ is gyromagnetic ratio which is a property of the different nuclei and is the length of time the field B_1 is on.

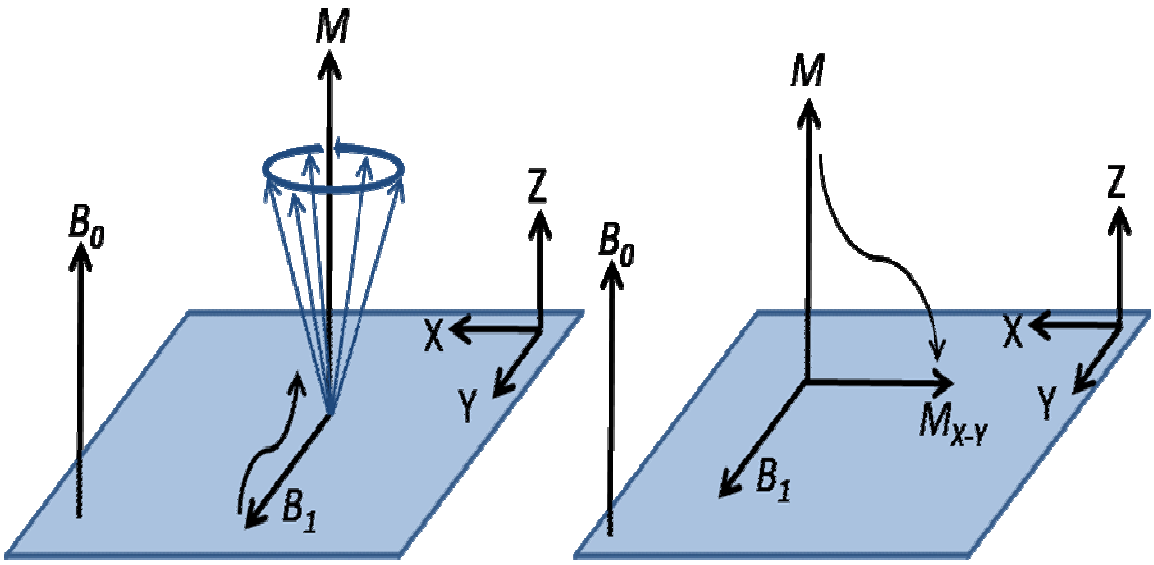

Figure 2.4: Illustration of the tipping of the magnetization vector *M* to the x-y plane in the presence of a 90 degree RF pulse B_1.

Once the B_1 field is turned off, the flipped magnetization will return to the equilibrium state and the projection of the magnetization on the longitudinal axis and transverse plane will be changed. This return to the equilibrium state is based on three factors, namely exchange of excess energy between the excited ^1H nuclei and the lattice, loss of phase coherence among spins due to the interactions between spins and loss of phase coherence among spins due to magnetic field inhomogeneity. The time constant that characterizes the rate of the projection of M_Z, which is the magnetization in longitudinal direction, based on the exchange of excess energy between the excited ^1H nuclei and the lattice is called the spin-lattice relaxation time T_1. The time constant that

characterizes the vector component of the magnetization in transverse plane based on the loss of phase coherence among spins due to the interactions between spins is called the spin-spin relaxation time T_2. The time constant that characterizes the vector component of the magnetization in transverse plane based on the effect of the inhomogeneity of B_0 on the phase of nuclear spins is called as T_2^* relaxation time. The relation between the gradual increase in M_Z and T_1 is given by equation (*2-3*).

$$M_z(t) = M(1 - e^{\frac{-t}{T_1}}) \tag{2-3}$$

T_1 is the time taken for M_Z to grow from 0 to approximately 63% of M following a 90 degree pulse (*Figure 2.5*). The relation between the gradual decay in M_{XY} and T_2 is given by the equation (*2-4*).

$$M_{xy}(t) = M \times e^{\frac{-t}{T_2}} \tag{2-4}$$

T_2 is the time it takes for the transverse magnetization M_{xy} to decay to 37% of its original magnitude (*Figure 2.6*).

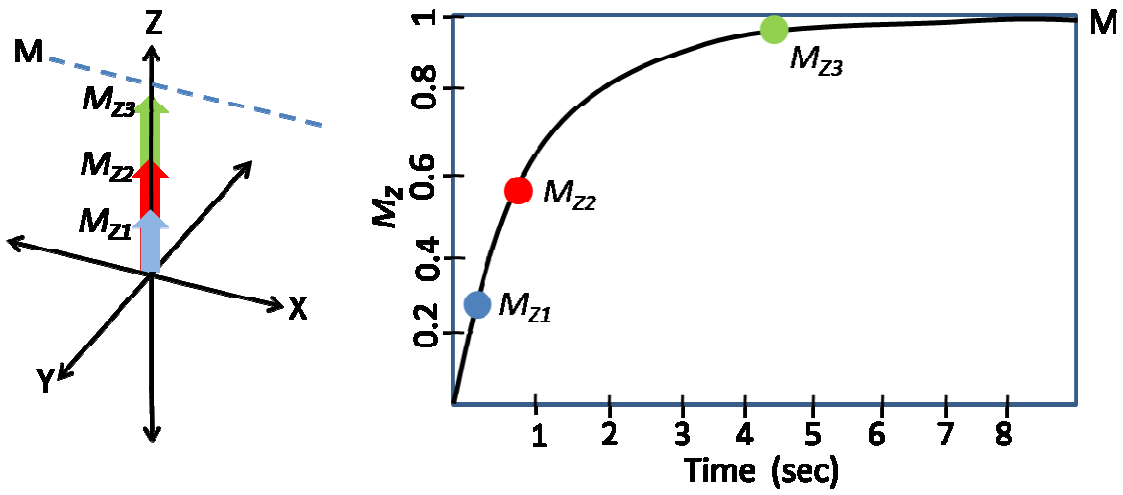

Figure 2.5: T_1 recovery curve showing the increase in M_Z over time.

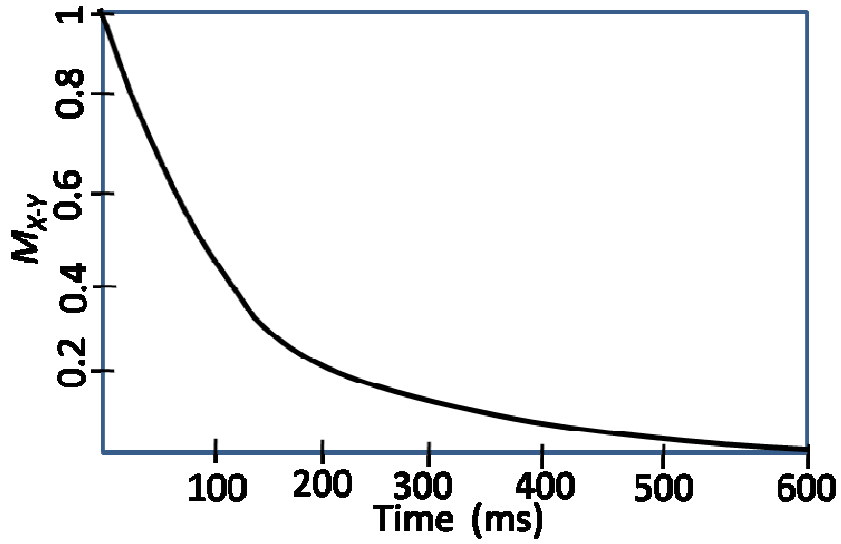

Figure 2.6: T_2 decay curve showing the decrease in M_{X-Y} over time.

Along with the concentration of the magnetization spins, these time constants are essential imaging parameters in MR imaging. The contrast between different tissues in an MRI image is achieved based on the different relaxation times of different tissues. When a RF receiver coil is placed in the vicinity of the rotating magnetization spins, according

to the Maxwell's equation, an alternating current is induced in the receiver coil, called as free induction decay (FID). This is the MR signal that is measured (*Figure 2.7*).

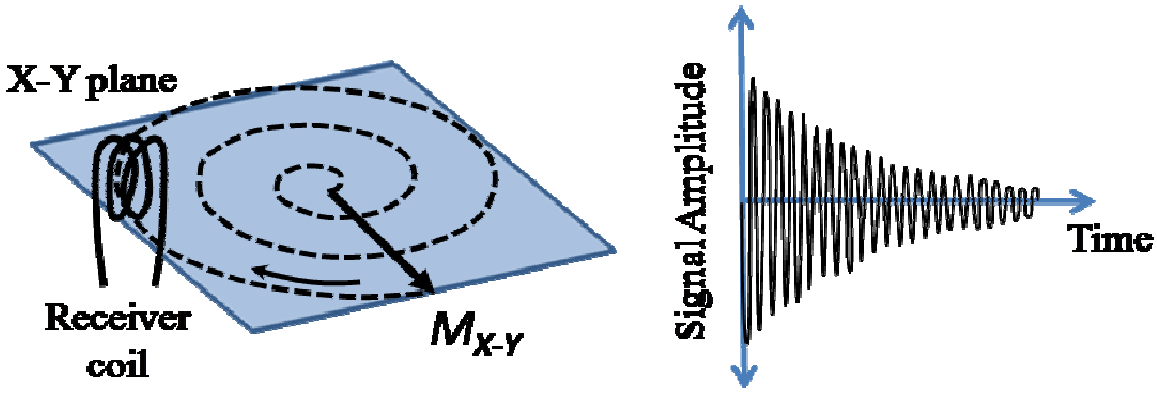

Figure 2.7: Free induction decay in the RF receiver coil due to the rotating magnetization spins in the X-Y plane.

In the FID signal described above, there is no spatial information, which is necessary to form the MR image. In order to incorporate spatial information, gradient coils need to be used to produce the spatial encoding gradients. Based on this, the main components of the MRI system are the main magnet that produces the homogenous B_0 field, the RF coil to emit the radiofrequency signal which is used to excite the nuclear spins, the gradient coils to produce the spatial encoding gradients and a RF receiver coil to amplify and measure the MR signal. The same RF coil can be used to transmit the RF pulse and receive the MR signal . The time sequence of the magnetic fields applied during an MRI scan can be described by a pulse sequence diagram. A spin echo pulse design is shown in *Figure 2.8*.

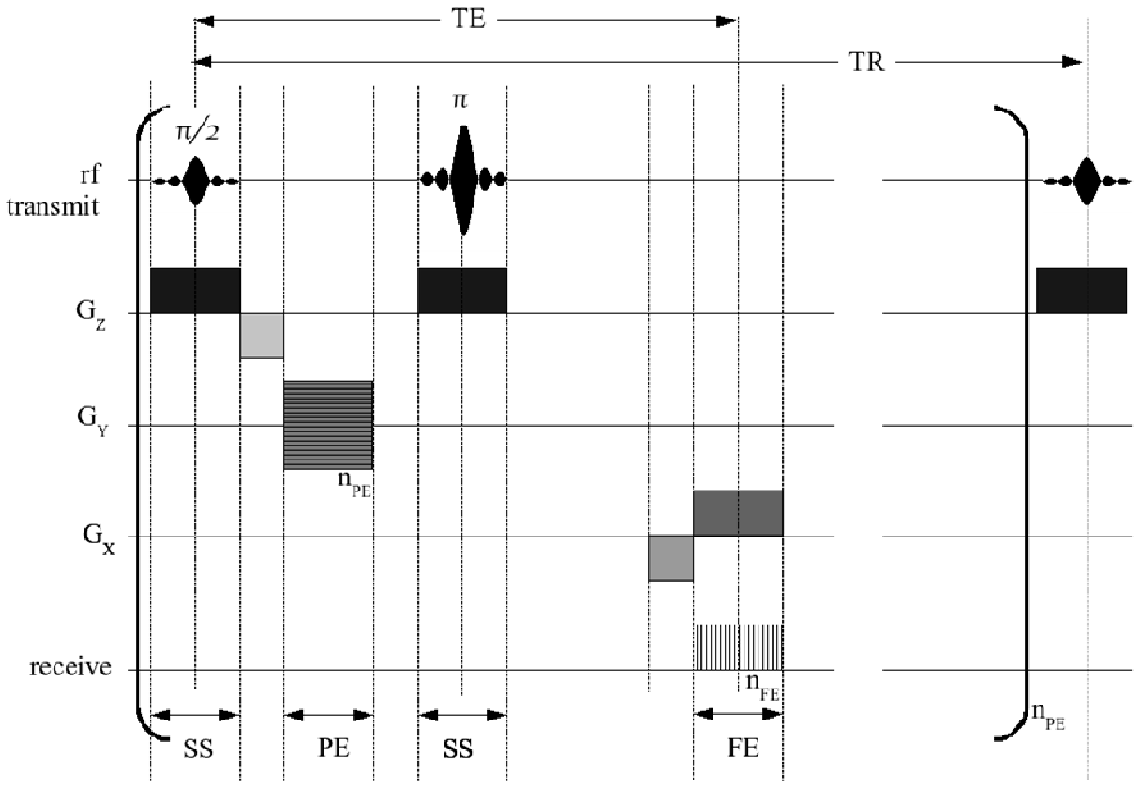

Figure 2.8: Spin echo pulse design. Here G_z is the slice selection gradient, G_y is the phase encoding gradient and G_x is the frequency encoding gradient. SS = slice selection, PE = phase encoding, FE = frequency encoding, n_{PE} = number of phase encoding steps, n_{FE} = number of readout steps, TE = echo time and TR = repetition time.

By choosing different scan parameters like echo time (TE) and repetition time (TR), different image contrast can be formed based on the relaxation properties of tissues. As a direct result, different tissues or pathological changes can be highlighted.

2.2 Diffusion Weighted Magnetic Resonance Imaging (DWI)

DWI is a magnetic resonance technique that measures and quantifies the attenuation of the MR signal due to diffusion of water molecules. The basic principle behind DWI is that a signal can be obtained that measures diffusion of water molecules in tissue. In a uniform system with no concentration gradients, the flux of water is dominated by molecular motion caused by thermal agitation. This leads to flux patterns created by small concentration gradients that are distributed randomly in an isotropic

medium. These flux patterns can be characterized by the diffusion coefficient *D* which relates the concentration gradient to the rate of transfer of water molecules through a unit area. The flux of water in one direction is related to the diffusion coefficient by the equation shown in (*2-5*).

$$F_x = -D\frac{\partial C}{\partial x} \tag{2-5}$$

Here F_x is the flux, *D* is the diffusion coefficient, *C* is the concentration of water and *x* is the length coordinate. The displacement of water molecules follows a Gaussian distribution. Einstein's equation (*2-6*) relates the mean displacement to the diffusion coefficient in one dimension,$\langle dr \rangle$.

$$\langle dr \rangle = \sqrt{2Dt} \tag{2-6}$$

Another factor influencing the diffusion coefficient of water molecules is kinematic velocity and temperature, as given by the Einstein-Stokes equation (*2-7*).

$$D = \frac{RT}{6\pi N v r} \tag{2-7}$$

Here *R* is the universal gas constant, *T* is the abolute temperature, *N* is Avogadros's number, *v* is the kinetic viscosity and *r* is the radius of the water molecule. Based on this, the diffusion coefficient of water is dependent on diffusion time, temperature and the local viscosity caused by water-protein electrical interactions, diffusion barriers and permeability.

The main principle behind DWI is attenuation of the MR signal due to diffusion of water molecules. In order to quantify this attenuation, DWI tags hydrogen atoms in

water molecules within certain tissue volume using diffusion sensitizing magnetic field gradients and then the resulting attenuation of the MR signal is measured after a time delay Δ. The typical RF pulses, spin dynamics and diffusion sensitizing gradients involved in a one dimensional spin echo DWI experiment are shown if *Figure 2.9*. The water molecules are first tagged using a dephasing gradient and then untagged using a rephasing gradient. During the diffusion time (Δ) between the tagging and the untagging, water diffuses in and out of the targeted volume causing a phase disruption in the spins as compared to the water molecules present originally at that location.

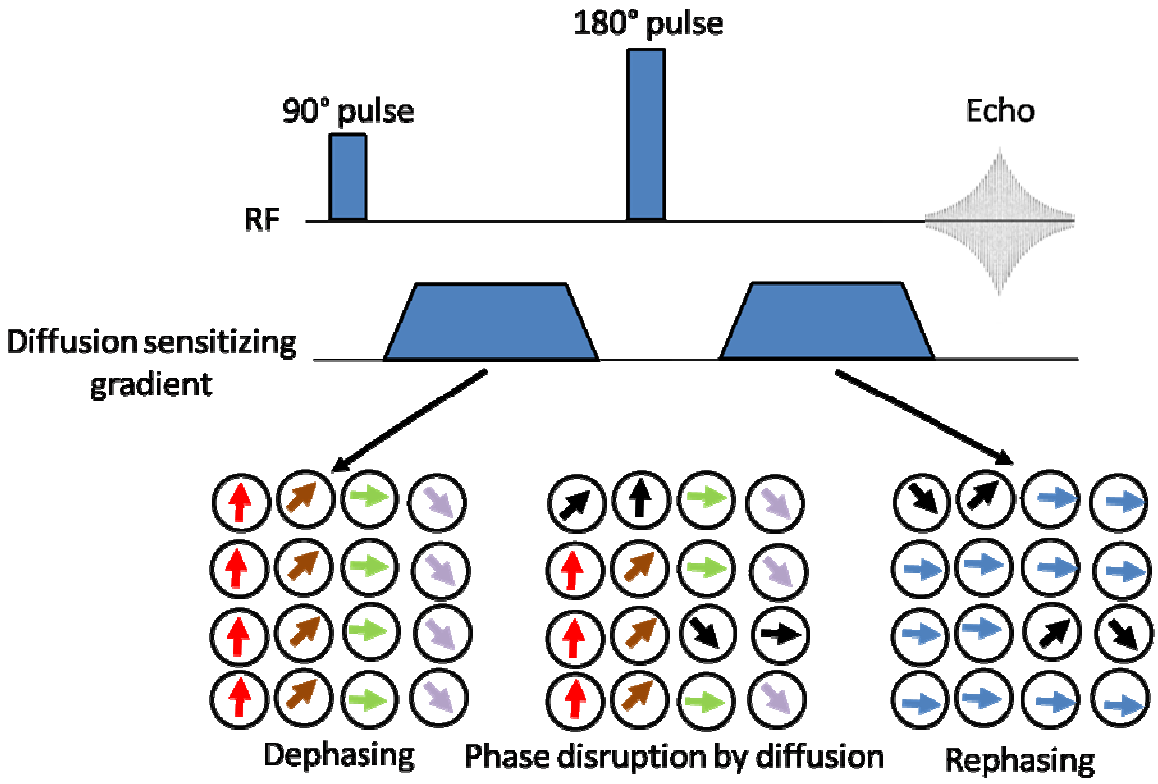

Figure 2.9: One dimensional spin echo showing one diffusion sensitizing gradient. The dephasing gradient tags the phase nuclear spins. The nuclear spins of the water molecules that undergo diffusion (marked by black arrows) show further phase disruption which is preserved when the rephasing gradient untags all the nuclear spins. This results in loss of MR signal.

This results in destructive phase interference and overall MR signal attenuation. The apparent diffusion coefficient is then calculated by quantifying the amount of signal attenuation after the application of diffusion sensitizing gradients as given by equation (*2-8*).

– (2-8)

Here, S_0 is the image magnitude before diffusion weighting, S is the image magnitude after diffusion weighting, D is the apparent diffusion coefficient and b is the amount of diffusion weighting which is given by equation (*2-9*).

$$b = \gamma^2 G^2 \left[\delta^2 \left(\Delta - \frac{\delta}{3}\right) + \frac{\varepsilon^3}{30} - \frac{\delta.\varepsilon^2}{6}\right] \quad (2\text{-}9)$$

Here, G and ε are the amplitude and the slew rate of the magnetic field gradients respectively, δ is the gradient duration, Δ is the diffusion time and γ is the gyromagnetic ratio for the nuclei.

2.3 Diffusion Tensor Imaging (DTI)

The diffusion tensor is a matrix that describes the diffusion of water in a medium with respect to a well-defined global coordinate system. The diffusion characteristics of an anisotropic medium is well characterized by the diffusion tensor. To construct the diffusion tensor, diffusion weighted images are measured in multiple directions. Three imaging gradients are used to apply the diffusion gradients in specific combinations to measure the one dimensional apparent diffusion coefficient in specific directions. These DWI measurements are used to estimate the 3 x 3 diffusion tensor field using regression. This tensor describes the preferred magnitude and orientation of the self diffusion of water. The diffusion tensor contains nine elements of which six are unique values as the tensor is symmetric. As a result, *Dxy* = *Dyx*, *Dxz* = *Dzx* and *Dyz* = *Dzy*. DWI data must therefore be obtained in a minimum of six sensitizing directions to determine the tensor values. In order to obtain a better estimate of the diffusion tensor, more diffusion sensitizing directions can be used. The diffusion tensor (*D*) is given in equation (*2-10*).

$$D = \begin{matrix} D_{xx} & D_{xy} & D_{xz} \\ D_{yx} & D_{yy} & D_{yz} \\ D_{zx} & D_{zy} & D_{zz} \end{matrix} \quad (2\text{-}10)$$

Once the diffusion tensor is created it is used to find the preferred diffusion magnitude and direction by calculating the eigenvalues and the eigenvectors of the tensor. The eigenvalues and the eigenvectors can be used to define the geometry of a diffusion ellipsoid which can be then used to visualize the diffusion tensor (*Figure 2.10*). The eigenvalues are used to define the magnitude of the axes of the ellipsoid and the eigenvectors are used to determine the orientation of each axis of the ellipsoid. The diffusion characteristics of each voxel are described by one ellipsoid.

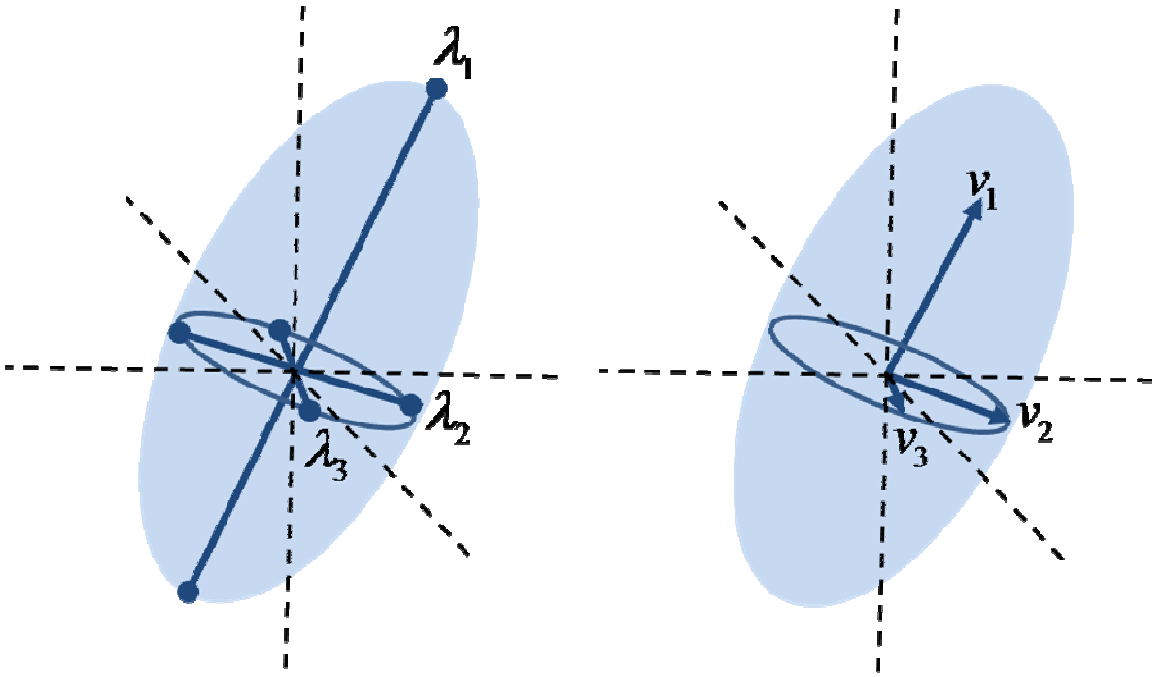

Figure 2.10: The eigenvalues and the eigenvectors of the diffusion ellipsoid.

The eigenvalues are also used to create DTI stains or indices. Examples of the DTI indices include longitudinal apparent diffusion coefficient (lADC), transverse

apparent diffusion coefficient (tADC), fractional anisotropy (FA), and mean diffusivity (MD). lADC reflects the diffusion parallel to axonal orientation and is given by equation (*2-11*).

$$\text{lADC} = \lambda_1 \tag{2-11}$$

Here λ_1 is the largest eigenvalue and represents the magnitude of the long axis of the diffusion ellipsoid. tADC reflects diffusion in the transverse plane and is given by equation (*2-12*).

$$\text{tADC} = \frac{\lambda_2 + \lambda_3}{2} \tag{2-12}$$

Mean diffusivity is defined as the average of all the three eigenvalues and defines the total diffusion in a given voxel. It is define as shown in equation (*2-13*).

$$\text{MD} = \frac{\lambda_1 + \lambda_2 + \lambda_3}{3} \tag{2-13}$$

FA indicates the degree of difference between isotropy and anisotropy and is given by the equation (*2-14*).

$$\text{FA} = \sqrt{\frac{3\left[\left(\lambda_1 - \lambda'\right)^2\left(\lambda_2 - \lambda'\right)^2\left(\lambda_3 - \lambda'\right)^2\right]}{2\left(\lambda_1 + \lambda_2 + \lambda_3\right)}} \tag{2-14}$$

DTI indices are derived based purely on the eigenvalues and don't incorporate the directional information contained in the eigenvectors. Although this shortcoming can be overcome by using diffusion ellipsoids to visualize diffusion, this method is not widely used in practice.

2.4 Anatomy and physiology of the spinal cord

2.4.1 Spinal cord anatomy

The spinal cord is the most caudal part of the central nervous system. It receives and processes sensory information from the skin, joints, and muscles of the limbs and trunk and controls movement of the limbs and the trunk. It is subdivided into cervical, thoracic, lumbar, and sacral regions. The spinal cord continues rostrally as the brain stem, which consists of the medulla, pons, and midbrain. The cross section of the spinal cord shows the presence of central gray matter, peripheral white matter and the central canal. The central canal is filled with cerebrospinal fluid. The gray matter contains neuronal cell bodies and synapses. The gray matter is divided into dorsal, ventral and lateral horns. The dorsal horn contains sensory relay neurons that receive input from the periphery, while the ventral horn contains motor nuclei that innervate specific muscles. The lateral horn contains visceral neurons. The white matter contains ascending and descending fiber tracts which are basically bundles of axons. The ascending tracts relay sensory information to the brain while the descending tracts relay motor instructions from the higher levels of the central nervous system.

2.4.1.1 White matter anatomy

The white matter (*Figure 2.11*)is divided into three paired funiculi; namely the dorsal funiculi, lying between the dorsal horns, the lateral funiculi and the ventral funiculi. Each funiculus has regions called fasciculi, which are nerve tracts. The ventral funiculus has both descending as well as ascending fasciculi. The descending ventral fasciculi include the ventral cerebrospinal, vestibulospinal and the tectospinal fasciculi.

The anterior cerebrospinal fasciculus consists of descending fibers which arise from cells in the motor area of the cerebral hemisphere of the same side and end by directly or indirectly branching around the motor cells in the anterior column. The vestibulospinal fasciculus is situated chiefly in the marginal part of the ventral funiculus and is concerned with equilibrium reflexes. The tectospinal fasciculus is situated partly in the ventral and partly in the lateral funiculus and is concerned with visual reflexes. The ascending ventral fasciculi include the ventral spinothalamic fasciculus and the ventral proper fasciculus. The ventral spinothalamic fasciculus is situated in the marginal part of the ventral funiculus. It ends in the thalamus and conducts certain touch impulses.

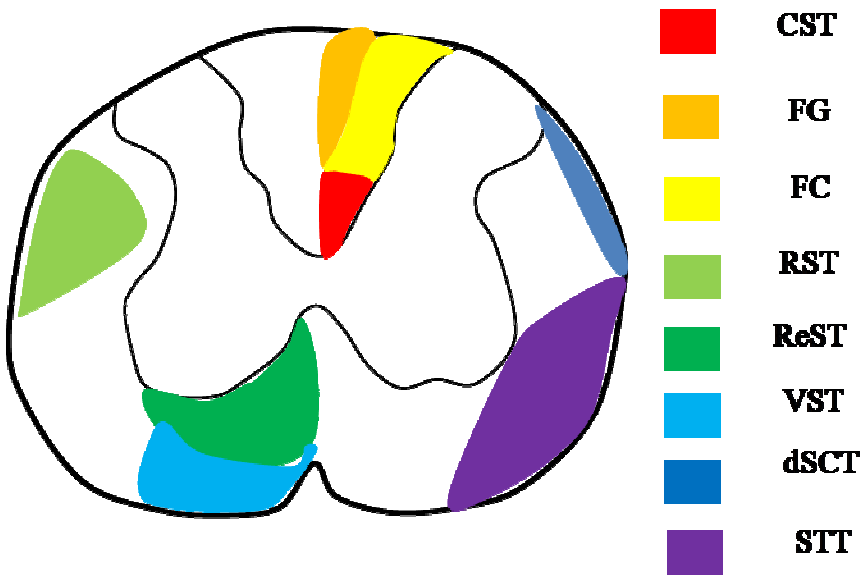

Figure 2.11: Principal fasciculi of the spinal cord. RST = rubrospinal tract, ReST = reticulospinal tract, VST = vestibulospinal tract, FG = fasciculus gracilis, FC = fasciculus cuneatus, CST = corticospinal tract, dSCT = dorasl spinocerebellar tract, STT = spinothalamic tract.

The lateral funiculus also has both descending as well as ascending fasciculi. The descending lateral fasciculi include the lateral cerebrospinal, rubrospinal and olivospinal fasciculi. The lateral cerebrospinal fasciculus arises from cells in the motor area of the cerebral hemisphere of the opposite side. The rubrospinal fasciculus lies on the ventral part of the lateral cerebrospinal fasciculus and descends from the mid-brain of the opposite side. The olivospinal fasciculus rises in the vicinity of the inferior olivary nucleus in the medulla oblongata and is present only in the cervical region of the spinal cord. The ascending lateral fasciculi include the dorsal spinocerebellar, ventral spinocerebellar, lateral spinothalamic, spinotectal, Lissauer and lateral proper fasciculi. The dorsal spinocerebellar fasciculus is situated at the periphery of the dorsal part of the lateral funiculus. The ventral spinocerebellar fasciculus is located at the periphery of the lateral funiculus in front of the dorsal spinocerebellar fasciculus. It begins about the level of the third pair of lumbar nerves and can be followed into the medulla oblongata and pons where it crosses over the superior peduncle and then passes backward along its medial border to reach the vermis of the cerebellum. The lateral spinothalamic fasciculus consists of axons of cells in the dorsal column and the intermediate gray matter which cross in the anterior commissure to the opposite lateral funiculus where they ascend and terminate in the ventro-lateral region of the thalamus. It conducts impulses of pain and temperature. The spinotectal fasciculus begins in the dorsal column and terminates in the superior colliculi. The fasciculus of Lissauer consists mainly of fine non-medullated fibers derived mostly from the dorsal roots. These non-medullated fibers play an important role in the reflexes associated with pain impulses.

The dorsal funiculus shows the presence of fasciculus gracilis and the fasciculus cuneatus. The fasciculus gracilis lies next to the posterior median septum. It consists of long thin fibers which originate in the posterior nerve roots and ascend to the medulla oblongata where they terminate in the nucleus gracilis. The fasciculus cuneatus lies between the fasciculus gracilis and the posterior column. It consists of larger fibers which originate in the posterior nerve roots. Some of these fibers ascend for only a short distance in the tract and come into close relationship with the cells of the dorsal nucleus in the gray matter while others ascend to the medulla oblongata where they terminate in the gracile and cuneate nuclei (Gray 1918).

2.4.1.2 Gray matter anatomy

The morphology of the spinal cord gray matter is heterogeneous in nature. However, the gray matter shows the presence of intrinsic organization based on which it can be divided into laminae. Rexed first described these laminae in cats (Rexed 1954). Based on this work, the concept of laminae have been used to describe cytoarchitecture in the mouse (Sidman, Angevine et al. 1971), rat (Paxinos 2004) and humans (Paxinos and Mai 2004). In rats, as well as in humans, there are ten laminae organized in layers going beginning at the dorsal horns and ending in the ventral horns. The structure and the size of the laminae vary based upon the spinal cord segment. This variation in the cervical spinal cord gray matter segments is shown in *Figure 2.12.*

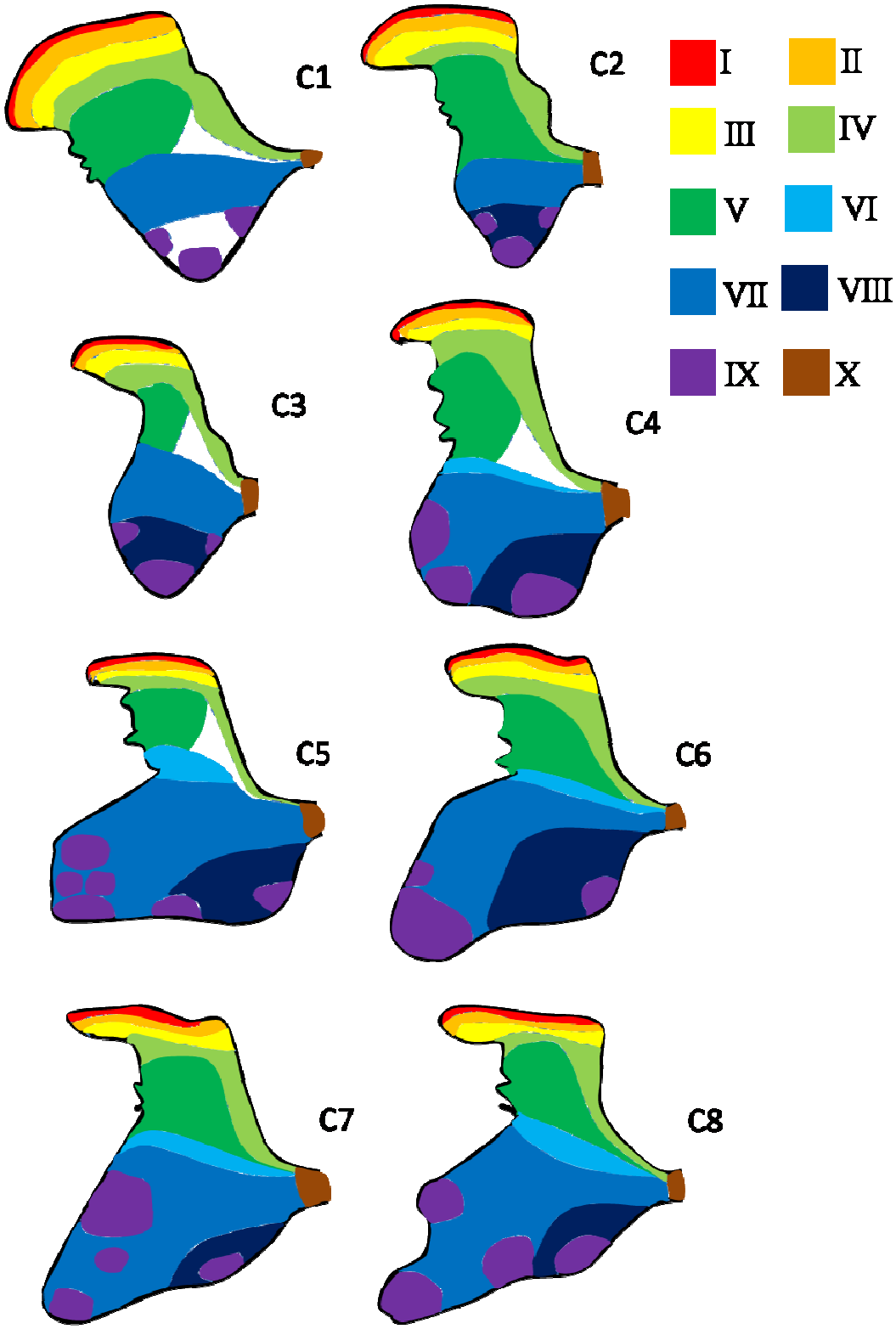

Figure 2.12: Rexed's laminae in the rat C1 to C8 cervical segments.

Lamina I is the most dorsal of the Rexed's laminae. It is a thin layer that covers the dorsal margin of the dorsal horn and bends laterally around its apex to also cover about half the lateral side of the head of the dorsal horn. Lamina I shows the presence of many myelinated nerve fibers which gives it a reticulated look. The neurons present in Lamia I are basically of four morphological types: fusiform, multipolar, flattened and pyramidal. The fusiform cell type is characterized by a spindle shaped cell body oriented in a longitudinal direction with two primary dendrites arising from the rostral and caudal poles. The mulitpolar cell has an ovoid shaped cell body from which several primary dendrites arise. The flattened neurons have a disc shaped cell body and have sparsely branched dendritic trees. The pyramidal neurons are triangular in shape and their dendrites typically arise from each corner of the cell body.

Lamina II lies ventral to the lamina I. Lamina II shows the presence of dense neurons. Lamina II follows the shape of lamina I in transverse sections, bending around the apex so that lamia I forms its lateral and dorsal borders. Lamina II is thicker than lamina I and does not have uniform thickness, with thickness being maximum medially in rodents. The two main cell types commonly found in lamina II are the stalked and the islet cells. The stalked cells are found mostly in the outer layer of lamina II. The stalked cells have a round or oval shaped soma with ventrally directed dendrites that stream out at oblique angles to form a cone shape. The islet cells are found throughout the lamina II in rats. The islet cells have very long dendritic trees extending along the rostrocaudal axis of the spinal cord.

Lamina III lies across the dorsal horn parallel with laminae I and II. Its border bends around the apex of the dorsal horn. It is bordered by the lamina II laterally and the

white matter medially. Lamina III is thicker than lamina I and II. Lamina III shows the presence of myelinated fibers which distinguishes it from lamina II. Lamina III shows the presence of rounded, slightly elongated or spindle shaped cells. The cells in lamina III are of similar size and density as compared to lamina II.

Lamina IV stretches straight across the base of the head of the dorsal horn and shows the presence of a medial bend in rats. Lamina IV is thicker than laminae I-III and is bordered by laminae I-III laterally and white mater medially. Lamina IV shows the presence of lower cellular density and larger cell size as compared to laminae I-III.

Lamina V is located at the neck of the dorsal horn. It shows the presence of thick nerve fibers. It shows the presence of triangular, star shaped and spindle shaped cells. The size of the cells are heterogeneous. Large cells are found in the lateral zone while small and medium sized cells are found in the medial zone.

Lamina VI is the deepest layer of the dorsal horn and is present only in certain regions of the spinal cord. It is prominent in regions of limb enlargements. It has a slightly curved ventral surface and is thickest in the medial portion. Lamina VI shows the presence of small, elongated, spindle shaped or triangular shaped cells along with large star shaped cells. A major function of cells in lamina VI is acting as interneurons involved in reflex pathways.

Lamina VII is commonly known as the intermediate gray matter and occupies a large area in the center of the gray matter. It extends medially to border lamina X and laterally to the later funiculus of the white matter. At the limb enlargements, the size of the lamina VII increases and reaches ventrally to the ventral border of the gray matter.

Lamina VII has a homogeneous appearance although it sometimes shows the presence of a few large star shaped cells resembling large motoneurons. Lamina VII also shows the presence of triangular, multipolar and fusiform shaped cells. The cells in lamina VII are interneurons that connect to the motoneurons in lamina IX.

Lamina VIII shows a variance in size and shape at different levels of the spinal cord. At the cervical and the lumbar enlargements, it is present in the medial base of the ventral horn. Everywhere else it extends across the whole base of the ventral horn. Some cells in the this lamina are very large and are almost appear similar to motoneurons. Lamina VIII is heterogeneous and also consists of spindle shaped cells.

Lamina IX is located at the base of the ventral horn. It shows the presence of motoneurons of the spinal cord. There are two prominent types of motoneurons. The alpha motoneurons are the largest of all cells in the spinal cord and are usually star-shaped. The gamma motoneurons are the smaller motoneurons present in lamina IX and account for 30% of the total number of neurons present in lamina IX. These cells present in lamina IX are organized into a series of longitudinal motor columns.

Lamina X is located around the central canal of the gray matter. To the dorsal side of the lamina X lies the lamina IV and to the ventral side lies the ventral white commissure. Lamina X is densely packed and consists of small triangular, spindle and star shaped cells.

2.4.2 Cells in the central nervous system (CNS)

Nerve cells and glial cells are the two types of cells in the CNS. Glial cells far outnumber neurons in the CNS. Glial cells support neurons and give structure and form. They also provide electrical insulation to neuronal groups and synapses. Glial cells are divided into microglia and macroglia. Microglia are phagocytes that are mobilized after injury, infection, or disease (Kandel, Schwartz et al. 2000). They arise from macrophages outside the nervous system and are physiologically and embryologically unrelated to the other cell types of the nervous system. Oligodendrocytes, Schwann cells, and astrocytes are the three types of macroglia (Fleming, Norenberg et al. 2006). Oligodendrocytes and Schwann cells are relatively small in size. Oligodendrocytes are found in the CNS while Schwann cells are found in the peripheral nervous system. Each of these cells tightly wind their membranous processes around the axon in a spiral way and thus form a myelin sheath around the axon. This helps in electrical insulation. Each oligodendrocyte envelops an average of fifteen axonal internodes. Astrocytes are the most numerous of glial cells. They are star shaped and have long processes which terminate in end-feet. Protoplasmic astrocytes are found in the gray matter and have many short branched processes. Astrocytes have important functions like providing nutrients to the cells on which they form end feet. They also form an end foot on the CNS blood vessels and cause their endothelial cells to form tight junctions thus creating the protective blood-brain barrier. Astrocytes are highly permeable to potassium ions. As a result they help to maintain the right potassium ion concentration in the extracellular space between neurons. This is important considering that repetitive firing of the nerve cells may create an excess of extracellular potassium that could interfere with signaling between cells in

the vicinity. Astrocytes also help regulate synaptic activities by removing neurotransmitters from synaptic zones after their release (Kandel, Schwartz et al. 2000). The neuron consists of three parts: the dendrites, the cell body and the axons. The cell body is the part of the neuron that contains the nucleus and surrounding cytoplasm. Most nerve cells have a spherical, large nucleus with a prominent nucleolus. The chromatin is finely dispersed. The cell body contains a highly developed rough endoplasmic reticulum. In appropriately stained neurons, the rough endoplasmic reticulum and the free ribosomes appear as basophilic granular substance called as Nissl bodies. The number of Nissl bodies varies according to neuronal type and functional state. They are particularly abundant in motor neurons which are the largest nerve cells in the spinal cord gray matter. The alpha motoneurons are the largest and are between 30 - 50 micrometers in diameter whereas the smaller gamma motoneurons are around 20 micrometers in diameter.

2.5 Phases of spinal cord injury (SCI)

The pathophysiology of SCI is biphasic, consisting of a primary and secondary phase of injury. A number of pathophysiological inflammatory processes are triggered by the primary mechanical injury leading to the prolonged secondary injury phase. The primary phase includes the immediate response whereas the secondary phase includes the primary acute, secondary acute, intermediate and chronic responses.

2.5.1 Immediate response

The immediate response spans the initial two hours post injury and represents the primary phase of injury in the biphasic SCI model (Norenberg, Smith et al. 2004). It

includes the traumatic mechanical disruption of spinal tissue through tears, shearing stress and compression (Shi and Pryor 2002). Vascular changes such as vasodilation and hemorrhage also occur (Tator and Koyanagi 1997). This results in an increase in the apparent diffusion coefficient. The immediate response is dominated by the results of the injurious event itself and causes spinal shock and instant loss of function at and below the level of injury (Ditunno, Little et al. 2004). The pathological changes in this immediate stage include a generalized swelling of the spinal cord accompanied by hemorrhaging in the central gray matter. The direct mechanical disruption of cell membranes and ischemia resulting from vascular disruption results in necrotic death of the cells in the gray matter. Interruption of the vasculature leads to hemorrhage in the white matter surrounding the injury site (Kakulas 2004). Also, hemorrhage and swelling combine to produce spinal cord ischemia that may extend for many spinal segments both rostral and caudal to the injury. This results in a significant decrease in the apparent diffusion coefficient (Sagiuchi, Tachibana et al. 2002). Pathophysiological processes like activation of microglial cells begin immediately following injury due to the upregulation of proinflammatory cytokines like TNF-α and IL-β (Pineau and Lacroix 2007). Levels of glutamate, which is an excitatory neurotransmitter, could also reach excitotoxic levels at the onset of injury (Wrathall, Teng et al. 1996).

2.5.2 Primary acute response

The primary acute response of SCI lasts between two to forty eight hours following injury. This phase marks the dominance of the secondary inflammatory response and is characterized by hemorrhage, increasing edema, and inflammation. The disruption of the microvasculature, global hypotension, and increased interstitial pressure

cause a prolonged hypoperfusion seen after injury (Tator and Koyanagi 1997). Ionic homeostasis and excitotoxicity contribute to the propagation of cellular injury by necrotic and apoptotic cell death of both neurons and glia. For example, loss of regulation of Ca++ ion concentration results in cell death (Farber 1990). Excitotoxicity is a result of the excessive activation of glutamate receptors leading to the influx of Na+ and Ca++ through the NMDA and Kainate receptors (Park, Velumian et al. 2004). Reactive oxygen species contribute to radical mediated injury. Lipid peroxidation is one of the main hallmarks of radical mediated injury and is a long lasting free radical reaction which causes membrane damage leading to cell lysis (Sakamoto, Ohnishi et al. 1991). There is also an increase in the permeability of the blood brain barrier. This rise in permeability initially occurs due to direct mechanical disruption of the endothelial cells and astroglial processes whereas later it is caused by inflammatory mediators known to have profound effects on vascular permeability (Schnell, Fearn et al. 1999). The primary acute response also includes infiltration of inflammatory cells and continuing activation of resident microglia at the site of injury. The inflammatory cells involved are microglia, T cells, neutrophils, and monocytes (Fleming, Norenberg et al. 2006). These cells upregulate inflammatory mediators like TNF-α and IL-β following SCI (Povlishock 1993). TNF-α and IL-β further the secondary injury as well as help in the removal of cellular debris and provide a suitable environment for regenerative growth (Fleming, Norenberg et al. 2006). Oligodendrocytes are highly sensitive to ischemic injury and undergo apoptosis following SCI due to the activation of the oligodendrocyte FAS receptors by activated microglia expressing FAS ligand (Casha, Yu et al. 2001). Axonal demyelination occurs due to the loss of oligodendrocytes, which peaks at around twenty four hours following injury in the

rat (Waxman 1989). Due to the loss of myelin, the fractional anisotropy decreases. Also, these inflammatory responses lead to an increase in the transverse component of the apparent diffusion coefficient (Ford, Hackney et al. 1994). This increase in the transverse diffusion is accompanied by a decrease in the longitudinal apparent coefficient.

2.5.3 Secondary acute response

The secondary acute response of SCI lasts between two days to two weeks following injury. The phagocytic response is most defined in this period. Phagocytes such as activated microglia and macrophages help in removing cell debris from the site of injury. They also promote axon growth to some extent through the removal of growth-inhibitory components. Along with the phagocytic response, astrocytes at the periphery of the lesion become hypertrophic and grow rapidly. Following this, the astrocytes express large cytoplasmic processes that interweave to form the gliotic scar which acts as a physical and chemical barrier to axonal regeneration. Reactive astrocytes express chondroitin sulfate proteoglycans which act as axonal growth-inhibiting molecules (Busch and Silver 2007). Astrocytes also play an important role in the regaining the homeostasis of ions and reestablishing the blood brain barrier which is important for alleviation of edema and controlling the infiltration of immune cells (Faulkner, Herrmann et al. 2004; Herrmann, Imura et al. 2008). The collagenous scar tissue affects the DTI eigenvectors and hence DTI tractography is sensitive to tissue scarring (Schwartz, Duda et al. 2005). Also, the influx of the microglia, the astrocytes and the macrophages leads to a decrease in extracellular volume which could lead to a decrease in the overall apparent diffusion coefficient.

2.5.4 Intermediate response

The intermediate response of SCI lasts between two weeks to six month following injury. Continued maturation of the astroglial scar and regenerative axonal maturation are the hallmarks of this response (Hill, Beattie et al. 2001).

2.5.5 Chronic response

The chronic response of SCI begins around 6 months after injury and continues throughout the lifetime of the injured subject. This response is characterized by Wallerian degeneration, astroglial and mesenchymal scar formation, schwannosis and development of cysts and syrinx. Wallerian degeneration is the rapid degeneration and atrophy of the portions of the nerve fibers which are separated from their cells along with little or no alteration in the cells and the parts of the fibers connected to them. It is characterized by distorted and fragmented myelin sheaths with absent or dense axoplasm. Eventually an astroglial scar replaces the destroyed myelinated axon (Ehlers 2004). The process of Wallerian degeneration of injured or severed axons is ongoing and it may take years for severed axons and their cell bodies to be fully removed. The astroglial scar is made up of tautly interwoven astrocyte processes attached to one another by tight junctions and is surrounded by extracellular matrix (Smith, Berry et al. 2001). The mesenchymal scar is the result of tissue healing and consists of fibrous connective tissue and collagen. This scar tissue presents a profound impediment to axonal growth (Norenberg, Smith et al. 2004). The chronic response also results in the formation of cysts which are cavities filled with extracellular fluid and commonly contain residual macrophages, small bands of connective tissue and blood vessels. These cysts provide a hindrance to regeneration

(Povlishock 1993). The syrinx is similar to the aforementioned cysts; the only difference being it has a denser gliotic wall. The pressure on the syrinx causes an enlargement of the cavity which results in compression of the adjacent spinal cord tissue and aggravation of neurological deficits. Schwannosis is an abnormal intramedullary and extramedullary proliferation of Schwann cells with associated axons. These cells are mostly derived from nerve roots that enter the cord and are caused mostly by incisive injuries. Most of the axons involved are unmyelinated. Wallerian degeneration could lead to changes in diffusivity even at locations distant from the injury site. This leads to an increase in transverse diffusion coefficients.

2.5.6 Morphological changes in gray matter

Axonal injury causes several changes in the cell body of the neuron. At acute stages the main changes in the morphology of the nucleus of the motor neurons includes shriveling of the nucleus and the presence of homogeneous eosinophilia of the cytoplasm. At chronic stages of injury the main changes in the morphology are the dissolution of the Nissl substance by a process known as chromatolysis, a decrease in the cytoplasmic basophilia, an increase in the volume of the soma and migration of the nucleus to the peripheral position in the soma. Chromatolysis is a precursor to the increase in protein synthesis by the neuron in order to restore the integrity of the axons after injury.

2.5.7 Neuroprotection and regeneration

Microglia provide trophic support to neurons and glia by releasing neuroprotective cytokines and growth factors (Nimmerjahn, Kirchhoff et al. 2005). Astrocytes are also sources of growth factors like NGF, FGF-2, PDGF, CNTF, IGF and

neurotrophic compounds. B lymphocyte cells provide neurotrophic factors. Autoantibodies specific for myelin protein promote axon regeneration and improve recovery (Huang, McKerracher et al. 1999). Macrophages derived from infiltrating monocytes produce neuroprotective cytokines and growth factors like TGF-β1 which limits oligodendrocytes toxicity (Merrill et al, 1991). This is followed by vascularization which occurs through angiogenesis (Norenberg, Smith et al. 2004).

2.6 Diffusion tensor imaging and its correlation to the injury response

It has been shown that gross morphological or MR imaging abnormalities of the spinal cord can be absent during the immediate phase with the exception of patients suffering from severe compressive or lacerative injuries (Aoyama, Hida et al. 2007). This calls for an imaging technique that is more sensitive to the underlying spinal cord microstructure than traditional imaging techniques. Diffusion tensor magnetic resonance imaging (DTI) has shown significant sensitivity to structural changes within the human spinal cord following acute spinal trauma and chronic spinal cord injury (Ellingson, Ulmer et al. 2006). Diffusion weighted imaging is a MRI technique that measures the attenuation of the MR signal due to incoherent motion or diffusion of unbound water molecules (Basser and Jones 2002). When a strong magnetic field gradient is present, the random motion of water molecules results in de-phasing of the MR signal which provides for the contrast in the DTI image (Le Bihan, Breton et al. 1986).

2.6.1 Spinal cord diffusion characteristics in health and injury

In the spinal cord, the white matter is significantly more anisotropic than the gray matter (Moseley, Kucharczyk et al. 1991). This diffusion anisotropy in white matter is

largely attributed to membrane diffusion barriers associated with axonal structures like neurofilaments, microtubules, cell membrane and myelin sheath restricting water diffusion to a preferred direction parallel to axon orientation. Transverse diffusion coefficients are reduced for axons with a smaller diameter, including axons both with and without myelin. Longitudinal diffusion coefficients vary directly with decreased myelin sheath thickness and axon diameter. Longitudinal diffusion also depends on neurofiliament and microtubule density, varying inversely with neurofilament and microtubule density (Beaulieu 2002).

DTI provides a non invasive measure that is sensitive to the nature and geometry of the underlying tissue microstructure. Thus, it provides insight into injury mechanisms and time course of pathological changes in spinal cord microstructure following trauma. There is a strong correlation between the MRI metrics and histology. The longitudinal diffusivity in the white matter tracts correlates well with the integrity of axons in those tracts (Kim, Budde et al. 2006). The transverse diffusivity in the white matter tracts correlate with the amount of myelin (Song, Yoshino et al. 2005). At the site of injury the apparent diffusion coefficient decreases due to inactivation of sodium and potassium pumps as a result of ischemia (Lu, Ashwell et al. 2000; Stanisz, Webb et al. 2004). Due to hemorrhaging, transverse diffusion increases and longitudinal diffusion decreases, decreasing the diffusion anisotropy while apparent diffusion increases (Deo, Grill et al. 2006). The extravasation of the inflammatory cells, the activation of microglia and hypertrophy of astrocytes results in a decrease of the extracellular water volume and the apparent diffusion coefficient. Cyst formation and atrophy during the chronic stage of injury also causes a decrease in extracellular volume that results in a decrease in

transverse diffusion coefficients in both the white matter and gray matter. Extracellular morphology also contributes to diffusion characteristics within the CNS. Higher axon density results in smaller transverse and longitudinal diffusion coefficients (Schwartz, Cooper et al. 2005).

The extensive use of DTI to study specific axonal tracts in the spinal cord white matter following spinal cord injury is in stark contrast to the lack of clarity with regards to diffusion parameters in the spinal cord gray matter. Diffusion characteristics in the spinal cord gray matter post injury have not been thoroughly explored. Although studies have been conducted to demonstrate significant changes in the overall spinal cord gray matter, to date there have been no studies correlating spinal cord gray matter cytoarchitecture to the DTI indices following spinal cord injury. Also, a firm understanding of the correlation between DTI characteristics in the cervical spinal cord gray matter and the underlying gray matter neuronal structure is yet to be established. Results from previous studies investigating the DTI characteristics in the white matter and the overall gray matter lend credence to the use of DTI for monitoring the status of the spinal cord gray matter post injury. However, more research is needed to fully understand the relation between the diffusion characteristics in the laminae of the gray matter post injury and the underlying morphological changes responsible for the changes in the diffusivity.

2.7 Image processing principles

In this study we attempt to select regions of interest in the cervical spinal cord gray matter based on histology templates. In order to do so both the histology and the

DTI images are pre-processed and post-processed using robust image processing techniques implemented both using custom algorithms as well as with standard image processing software. The principles behind the image processing techniques implemented in this study are explained in the following paragraphs.

2.7.1 Mathematical morphology

Mathematical morphology is a technique used to analyze digital images based on mathematical concepts from set theory. This techniques includes a wide range of operators used for the analysis of binary images in order to perform image enhancement, image segmentation, edge detection and noise removal. The image on which morphology is to be performed and the structuring element are the two inputs that these operators basically require. The structuring element is used as a probe to detect information in the image. The structuring element consists of a pattern of discrete points relative to some origin in the Cartesian coordinate system. *Figure 2.12* shows some examples of structuring elements. The two fundamental operators in mathematical morphology are erosion and dilation.

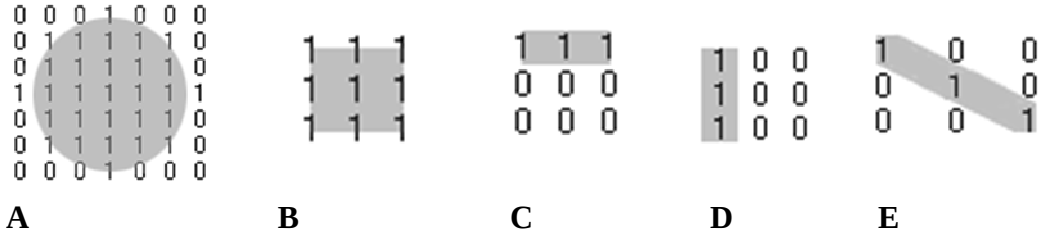

Figure 2.12: Examples of structuring elements. A) Disk-shaped structuring element. B) Square structuring element. C) Horizontal line structuring element. D) Vertical line structuring element. E) Diagonal structuring element.

2.7.1.1 Erosion

Erosion is a morphological operator that shrinks the objects in an image by removing pixels from the boundaries of objects. The mathematical definition of erosion for binary images is as follows: The erosion of A by B, denoted by A □ B

$$A \square B = \{ z \mid (B)_z \cap A^c \neq \emptyset \}$$

The erosion of A by B is the set of all structuring element origin locations where the translated B has no overlap with the background of A. Here A is the image, ∅ is the empty set and B is the structuring element. The manner and extent of erosion is controlled by the structuring element.

2.7.1.2 Dilation

Dilation is a morphological operation that grows or thickens objects in a binary image. The mathematical definition of dilation of binary images is as follows: The dilation of A by B, denoted by $A \oplus B$

$$A \oplus B = \left\{ z \mid \widehat{(B)_z} \cap A \neq \emptyset \right\}$$

Here A is the image, ∅ is the empty set and B is the structuring element. The dilation of A by B is the set consisting of all structuring element origin locations where the reflected and translated B overlaps atleast some portion of A. The manner and extent of dilation is controlled by the structuring element.

2.7.1.3 Morphological opening

The morphological opening of A by B denoted by A ◦ B is erosion of A by structuring element B followed by dilation of the result by B. The effect of the operator is to preserve foreground regions that have a similar shape to the structuring element, or that can completely contain the structuring element, while eliminating all other regions of foreground pixels. It also smoothes object contours, breaks thin connections and removes thin protrusions.

2.7.1.4 Morphological closing

The morphological closing of A by B denoted by A · B is dilation of A by structuring element B followed by the erosion of the result by B. The effect of the closing operator is to preserve background regions that have a similar shape to the structuring element, or that can completely contain the structuring element, while eliminating all other regions of background pixels. Morphological closing tends to smooth the contours of objects. It also joins narrow breaks, fills long thin gulfs and fills holes smaller than the structuring element.

2.7.2 Image registration

Image registration is the process of estimating an optimal transformation between two images in order to geometrically align the two images. Given two images denoted by I_1 and I_2, the mapping between images can be expressed as:

$$I_2 = g(T(I_1))$$

where T is the spatial transformation, and g is the intensity transformation function. For 3D medical images, T can be a 3D spatial coordinate transformation, which maps three spatial coordinates, x, y and z, to new spatial coordinates x', y' and z'.

$$(x'; y'; z') = \mathrm{T}(\mathrm{x};\ \mathrm{y};\ \mathrm{z})$$

while g maps the intensity of image I1 to corresponding intensity of image I2.Therefore g maps an image to an image while T maps between coordinates. The methods of registration in medical imaging can be classified as being landmark-based, surface-based or voxel-based (Jenkinson and Smith 2001). Landmark-based registration is based on the identification of corresponding landmarks on the two images. These landmarks can be either anatomical structures or external markers attached to the patient (Lemieux, Kitchen et al. 1994). Landmark-based registration methods achieve their target by minimizing the distance between corresponding points. This method is user-intensive as the accuracy of the method depends upon the accurate indication of the corresponding landmarks in the images by the user. In surface based registration, corresponding surfaces in the two images to be registered are delineated and a transformation is computed that minimizes the distance between the two surfaces. These segmentation methods are highly application and data dependent. Voxel-based (VSB) registration methods optimize a function, such as a correlation coefficient or an absolute sum of differences, measuring the similarity of all geometrically corresponding voxel pairs for some feature. The main advantage of VSB methods is that they are not limited by segmentation errors as in surface based methods because feature calculation is straightforward or even absent when only grey-values are used. This method of image registration is not as useful in registering images from different modalities as the corresponding voxel intensity values

are usually not related in different modalities. For intramodality registration, maximization of mutual information of voxel intensities within overlapping parts or in a region of interest (ROI) has been feasible. Overall, the main components involved in the process of image registration are the reference and the target images, feature detection and matching, the transformation model and the cost function.

2.7.2.1 Variations in images

The reference and the target images may vary from each other due to the following three major causes. The images may vary due to differences in acquisition which leads to a spatial misalignment. The images may also vary due to variations in the image intensity due to lighting conditions. Finally, variations between the images are introduced due to inherent changes in the object being imaged due to object movement or growth. Variations can be introduced due to images captured at different times in multitemporal analysis or images captured using different sensors in multimodal imaging. Variations also exist between a real world image of an object and an image of the model of the object. The different components of the image registration process are based on the types of variation between the reference and the target image.

2.7.2.2 Feature detection and matching

Significant and distinctive objects like region boundaries, curves and points are detected as features of the reference and the target image in order to match them. These region features are generally high contrast regions. They can be selected manually or automatically. For automatic feature detection, segmentation methods are used in order to extract the region boundaries. Also, the centroid of a closed boundary region can be used

to detect points in the image. The detected features in the reference and the target images are then matched using image intensity values in a certain defined neighborhood.

2.7.2.3 Transformation model

Following feature matching, images are mapped to new coordinates using a transformation model. Rigid, affine and non rigid are the different transformation models of interest. Rigid transformation is used when there is no distortion among images. A 3-D rigid transformation is composed of three rotations and three translations whereas a 2-D rigid transformation is composed of a rotation and two translations. It is a linear operation and can be represented by a 4x4 matrix in the 3-D case. The affine transformation is used when there is gross distortion in the target image as compared to the reference image. The affine registration is normally used as a crude approximation to a fully non-rigid transformation. A 3-D affine transformation is composed of three rotations, three translation, three stretches and three shears whereas a 2-D affine transformation is composed of a rotation, two translations, two stretches and two shears. The affine registration is a linear operation and can be represented by a 4x4 matrix in the 3-D case. The non rigid transformation is used for inter subject registration and for correction of distortion. It is a non linear transformation.

2.7.2.3 Cost function

Cost functions are used to determine the similarity between regions of interest in the reference and the target images. Intensity based methods and feature based methods are the two main types of cost functions. Intensity based methods use the intensity of pixels to quantify the difference between the registered and the target image. Sum of

squared differences, normalized correlation and mutual information are the different intensity based cost functions. Feature based methods compute cost as the distance between features in the registered and the target image.

Chapter 3:

Correlation of diffusion tensor imaging indices with histological parameters in rat cervical spinal cord gray matter following distal contusion spinal cord injury

3.1 Introduction

Diffusion tensor imaging (DTI) is continuing to emerge as a preferred technique for identifying structural changes in the spinal cord after trauma or with progressive disease; however, the vast majority of investigations have focused on diffusion properties that depend on white matter structure. For example, DTI reflects differences in axon spacing and axon diameter in healthy spinal cord white matter (Schwartz, Cooper et al. 2005). In pathological situations, demyelination is associated with an increase in transverse (radial) diffusion (Song, Sun et al. 2002; Song, Sun et al. 2003; DeBoy, Zhang et al. 2007; Hofling, Kim et al. 2009) while a decrease in longitudinal (axial) diffusion reflects axonal loss (Song, Sun et al. 2003; DeBoy, Zhang et al. 2007; Kozlowski, Raj et al. 2008; Budde, Xie et al. 2009; Hofling, Kim et al. 2009). Thus, DTI parameters can be useful in identifying loss in white matter integrity, especially at the site of the injury. Less is known about changes in diffusion distant from the injury and the effects of injury on the diffusion properties of spinal cord gray matter are largely unexplored.

Most investigations of spinal cord DTI have focused largely at the site of a lesion despite the liklihood that there are also changes in cellular structure substantial distances from the injury location. Diffusion and diffusion anisotropy of the white matter at the site of injury differ from other regions of the spinal cord (Deo, Grill et al. 2006; Tu, Kim et al. 2010), reflecting corresponding histological changes near the injury (Budde, Kim et al. 2007; Kozlowski, Raj et al. 2008). While some effort has been made to use DTI to track the propagation of changes in axon degeneration in white matter rostral and caudal to the injury (Narayana, Abbe et al. 1999; Deo, Grill et al. 2006) the extent of the spatial

changes has been limited largely to about 10 mm. Since the loss of axons and subsequent changes in white matter tracts propagate throughout the cord, changes in DTI parameters might also be expected at sites distant from an injury site. Evidence from DTI studies in humans has indicated that there are changes in diffusion in the spinal cord white matter even in regions remote from the injury (Ellingson, Ulmer et al. 2006; Ellingson, Ulmer et al. 2006; DeBoy, Zhang et al. 2007). Thus, changes in diffusion values are not concentrated at the lesion but are widespread through the spinal cord. Both longitudinal and transverse diffusivity show a general decrease throughout the spinal cord in human subjects with chronic SCI (Ellingson, Ulmer et al. 2008).

In addition to axonal loss and degeneration, SCI appears to affect the gray matter regions of the spinal cord. Morphological changes have been observed in the neurons in the gray matter, at the injury site as well as regions caudal to the injury site. These changes include an increase in the frequency of large motor neurons and an increase in the thickness of the dendritic bundles (Bose, Parmer et al. 2005). Changes in the dendritic structure of motoneurons caudal to the site of injury have also been observed following SCI in the rat (Kitzman 2005). In addition, the soma size of sympathetic preganglionic neurons of the lubrosacral spinal cord decreases with the loss of synaptic connectivity after SCI (Krassioukov and Weaver 1996). DTI parameters of intact rodent spinal cord gray matter have been characterized (Madi, Hasan et al. 2005; Ellingson, Kurpad et al. 2008; Kim, Haldar et al. 2009), although the effects of gray matter histological structure of the various lamina on DTI parameters has not been investigated. Further, while diffusivity of water is reduced in the gray matter in chronic SCI humans

rostral to the injury site (Ellingson, Ulmer et al. 2008), the histological features of spinal gray matter that underlie these diffusion changes are unknown.

In the current study, we examined the ex vivo diffusion characteristics in the cervical spinal cord gray matter following a T8 contusion SCI in the rat and examined the corresponding histological features at 2, 15 and 25 weeks post injury. We hypothesized that DTI would detect changes in the diffusion characteristics in the rat cervical spinal cord gray matter remote from the lesion during long-term recovery from traumatic SCI. We also hypothesized that DTI values in the rat cervical spinal cord gray matter would correlate to the size of the motoneurons of the cervical spinal cord gray matter in chronic SCI at T8.

3.2 Materials And Methods:

3.2.1 Animals

A total of twenty female Sprague-Dawley rats were used in this study. The animals were divided into the following four groups: an uninjured control group (n = 5, age = 8 weeks), an injured group allowed to survive two weeks post spinal cord injury (n = 5, age = 10 weeks), an injured group allowed to survive fifteen weeks post spinal cord injury (n = 5, age = 23 weeks) and an injured group allowed to survive twenty five weeks post spinal cord injury (n = 5, age = 33 weeks).

3.2.2 SCI model

A regulated, moderate contusion injury was induced in all the injured samples. Female Sprague-Dawley rats (200–250 g) were anesthetized with interperitoneal (IP)

Ketamine (75 mg/kg body weight) and Medetomidine IP (0.5 mg/kg body weight). An incision was made over the mid-thoracic region, subperiosteal dissection performed and a laminectomy over three levels (T7–T9) was performed to expose the spinal cord and overlying dura under sterile conditions. In order to induce a spinal contusion, an impactor (10 g) was dropped from a height of 25 mm directly onto the dura at the T8 level. This caused a moderate, incomplete spinal cord injury that is known to produce paraplegia or high-grade paresis. After impact, the wound was closed in layers. Postoperatively, animals were placed on a warm blanket, placed on enrofloxacin (10 mg/kg body weight, subcutaneous injection), and given lactated ringers subcutaneously (50 mL/kg body weight). The uninjured control animals did not receive any surgical procedures.

3.2.3 Ex vivo MRI

At the predesignated time post injury, an overdose of sodium pentobarbital (100 mg/kg body weight) was used to euthanize the animals before performing ex vivo MRI. Once the thoracic cavity was opened, a perfusion catheter was inserted into the ascending aorta, the right atrium was incised, and 300 mL of warm phosphate-buffered saline (PBS) was perfused to clear blood from the vasculature. Following this, fixation was achieved using 600 mL, 10% formalin (pH 7.4) at room temperature. The spinal cord was then extracted, macroscopically assessed and post-fixed in 10% formalin for up to 2 weeks. After post-fixation, each spinal cord was cut at the medulla and embedded in agarose gelatin (20 g of purified agarose + 500 mL dH_2O) within 2.5 cm diameter plastic, MR-compatible test tubes. In order to achieve proper alignment of each spinal cord, the

distance from the opening of the test tube to the medulla and the distance from the opening of the test tube to the lesion site were kept consistent across all the specimens. Temperature of the agarose gelatin was monitored continuously until the gelatin dissolved and liquefied. Spinal cords were not placed into the gelatin mixture until the temperature of the mixture cooled to less than 45°C to decrease the probability of protein denaturation. Spinal cords were removed from the agarose gelatin within twenty four hours of initial embedding. A total of four spinal cords were analyzed in each of the control, two week post injury, fifteen week post injury and twenty five week post injury groups.

The cords in the test tubes were bundled together and placed into a 9.4 Tesla (T), horizontal bore MR spectrometer (9.4T Bruker BioSpec 94/30 USR In vivo Spectroscopy Imaging System; Bruker BioSpin). A quadrature volume coil was used for radiofrequency excitation/reception. A single T2-weighted image ($b = 0$ s/mm^2) and six diffusion weighted images (DWIs) with non-collinear sensitizing directions were acquired at echo time/repetition time = 31.6 ms/14s, slice thickness of 2 mm with 1 mm interslice gap, field of view = 5.12 cm, NEX = 1, and an acquisition matrix of 512 x 512 using a standard pulsed gradient spin-echo (PG-SE) DW sequence. This produced DTI images with 100 µm in-plane resolution. In addition, DWIs had $\delta = 3$ ms, $\Delta = 15$ ms, and b-values ranging from 493.5–500.7s/mm^2 (target b-value = 500s/mm^2) depending on orientation of diffusion sensitizing gradients with respect to imaging gradients.

3.2.4 DTI Processing

In order to construct the diffusion tensor from the DWIs, the DWIs and the T2-weighted images were first imported into AFNI (http://afni.nimh.nih.gov/afni). The DWIs were coregistered with the T2-weighted images in AFNI using a Fourier transform- based, 6 degree of freedom, rigid-body registration algorithm to correct for eddy-current and susceptibility distortions. These coregistered DWIs were then exported to Matlab (MathWorks, Inc, Natick, MA) using the AFNI Matlab Library functions. The effective b-value, actual gradient directions calculated by the Bruker™ system and the image registration transformation matrix were also imported into Matlab to accurately construct the tensor.

Once the diffusion tensor was constructed it was used to calculate the DTI parameters. The DTI parameters used in this study were the longitudinal apparent diffusion coefficient (lADC), transverse apparent diffusion coefficient (tADC), mean diffusivity (MD) and fractional anisotropy (FA). lADC was defined as the largest eigenvalue, tADC was defined as the average of the two smallest eigenvalues, MD was the average of all three eigenvalues and fractional anisotropy was calculated as defined by Pierpaoli and Basser (Pierpaoli and Basser 1996). All DTI parameters were calculated in Matlab and saved for further analysis.

3.2.5 Histological staining

3.2.5.1 H & E staining for registration

In order to perform registration of DTI images to the corresponding histology, tissue sections with eriochrome cyanine R stain and H&E counter-stain were obtained. Following ex vivo imaging, samples from each subject in the control (n = 4) , two weeks post injury (n = 4), fifteen weeks post (n = 4) and twenty five weeks post injury (n = 4) groups were dehydrated, blocked in paraffin, sliced axially and stained with eriochrome cyanine R stain and H&E counter-stain. Axial slices of the cervical spinal cord were digitally imaged at 4x magnification using a Nikon Eclipse E600 research microscope (Nikon Instruments, Inc, New York) and the images were captured with a Diagnostic Instruments CCD digital camera (Diagnostic Instruments, Inc, Sterling Heights, MI) using SPOT image acquisition software (Diagnostic Instruments, Inc, Sterling Heights, MI) (Figure 3.1).

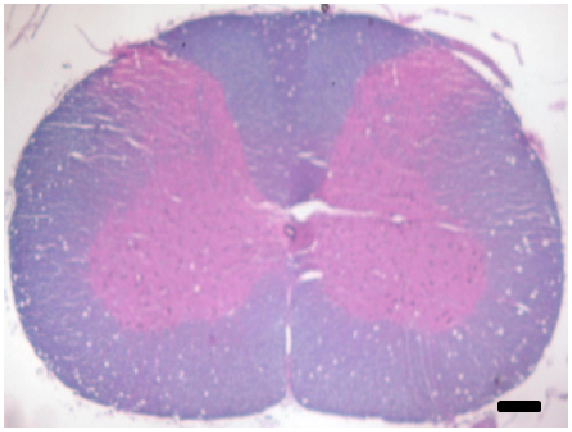

Figure 3.1: Cervical spinal cord axial slice stained with eriochrome cyanine R and counter-stained with H&E captured at 4x magnification. Scale bar = 200 µm. Note that these images produced an obvious color delineation between white matter and gray matter.

3.2.5.2 Toluidine blue staining for structural changes

Tissue samples adjoining the sections used for the eriochrome staining were postfixed in osmium tetroxide (OsO_4) and toluidine blue histological staining was used to identify evidence of ongoing changes in the cervical spinal cord gray matter for control (n = 4), two weeks post injury (n = 4) and twenty five weeks post injury (n = 4). OsO_4 and toluidine blue histological processing was conducted off-site, at the Central Microscopy Research Facility at the University of Iowa, using a similar protocol to Schwartz et al. (41). The protocol consisted of washing the tissue in a phospate buffer, post- fixing the tissue for 1-2 hours in 1% OsO_4 in buffer, washing the tissues in a buffer rinse and dH_2O rinse, and then dropping the processed tissue into 2.5% uranyl acetate for approximately 20 minutes. After dehydration, infiltration began with washes of ethanol followed by washes of EPON epoxy resin. After complete immersion in EPON the tissue was cut into 1 µm sections and stained with toluidine blue. Slides were then coverslipped for light

microscopy. Axial slices of the cervical spinal cord were digitally imaged at 4x magnification along with regions of interest in the gray matter which were digitally imaged at 40x magnification. A Nikon Eclipse E600 research microscope equipped with a Diagnostic Instruments CCD digital camera interfaced with SPOT image acquisition software was used for capturing the images (Figure 3.2).

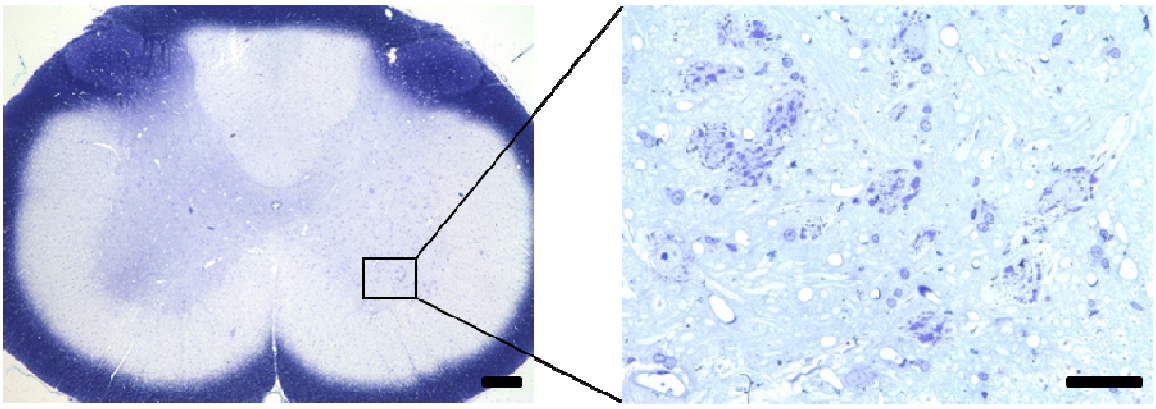

A **B**

Figure 3.2: A) Cervical spinal cord axial slice of an uninjured control rat stained with Osmium tetroxide (OsO_4) and toluidine blue captured at 4x magnification. Scale bar = 200 µm B). Image of the Region of Interest (ROI) in the gray matter captured at 40x magnification. Scale bar = 50 µm.

3.2.6 Region of Interest Selection

Histological templates were used to automatically select gray and white matter regions of interest (ROIs) in the DTI maps of a each specimen. The histology templates were constructed from a histological section of the spinal cord stained with eriochrome cyanine R stain and H&E counter-stain. The axial slice of the DTI within the cervical spinal cord that best resembled the cord morphology of the histological image was used for analysis of each sample. The cervical segments selected in all the subjects were from

the C4 - C6 level except for two subjects in the two weeks post injury group for which they were selected from the C1-C2 level. Before mapping the histology templates onto the DTI maps, the DTI maps were registered to the histology templates using whole cord images obtained from both histology and DTI, as described in the following sections.

3.2.6.1 Histology segmentation

To begin, the white matter, the gray matter and the entire spinal cord in the histology image were segmented using a custom cluster analysis algorithm written in Matlab. In order to classify the regions into white matter, gray matter and the whole spinal cord, three sample ROIs were drawn manually in the RGB images. These samples were selected randomly, one each from the white matter, the gray matter and the background. The RGB image was then converted into the L*a*b* color space (Figure 3.3a & 3.3b). Mean values of the chromaticity layers a* and b* were calculated in each sample ROI, and then the mean values used to define markers for the regions containing the white matter, gray matter and background. In order to classify the pixels into three regions, a Euclidean distance measure was calculated between each pixel and each region marker. Using minimum distance as a classification factor, each pixel was then labeled as either white matter, gray matter or the background (*Figure 3.3c*). These pixel labels were then used to segment the RGB image into white matter, gray matter and background.

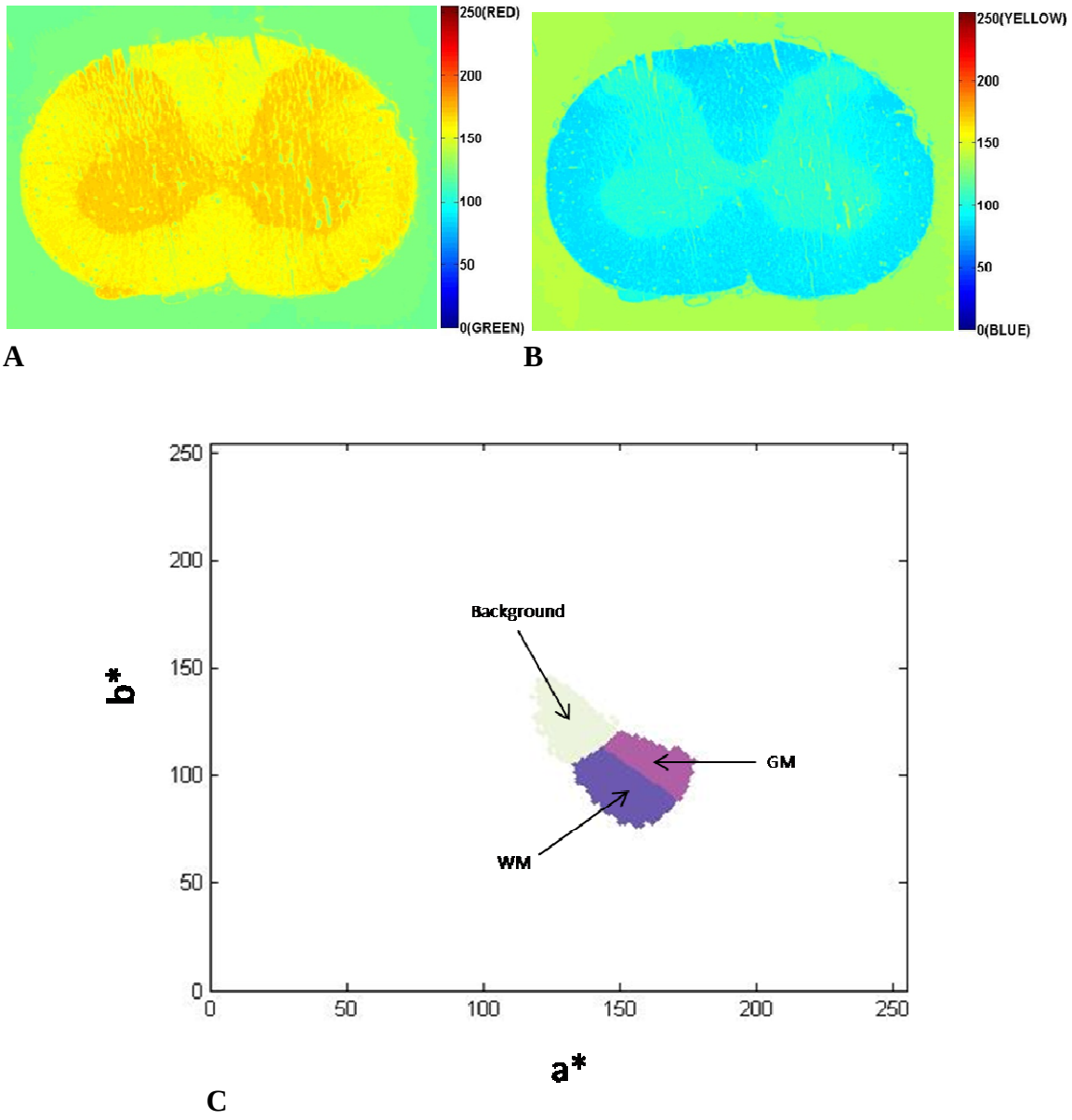

Figure 3.3: A) Chromaticity layer a* of the L*a*b* color space. The color bar represents the position of the color of the pixels between green and red. B) Chromaticity layer b* of the L*a*b* color space. The color bar represents the position of the color of the pixels between blue and yellow. C) Scatterplot of the segmented pixels in a*b* space showing pixels classified as background, white matter (WM) and gray matter (GM).

3.2.6.2 Histology template formation

The segmented regions were then used to form histology templates of the white matter, the gray matter and the whole cord. In order to form the whole cord template, image thresholding was first used to convert the RGB image containing the region segmented as background into a binary image, which was then inverted. Gaps in the border of the binary template were closed using image dilation. Once the gaps were closed, region filling was used to fill holes in the whole cord template. This was followed by image erosion in order to make the whole cord template smooth. The RGB images containing the region segmented as white matter and gray matter were used to form templates of the white matter and the gray matter respectively using the same process, except that the binary image was not inverted. The center of mass of the whole cord template, which coincided approximately with the central canal, was then found and aligned with the center of the image frame. The image frame was then zero padded to obtain a 1:1 aspect ratio and an image size that was an exact power of two while keeping the center of mass of the whole cord template aligned with the center of the image frame. The white matter template, the gray matter template and the L*a*b* histology image were then similarly aligned with the center of their respective image frames (*Figure 3.4*).

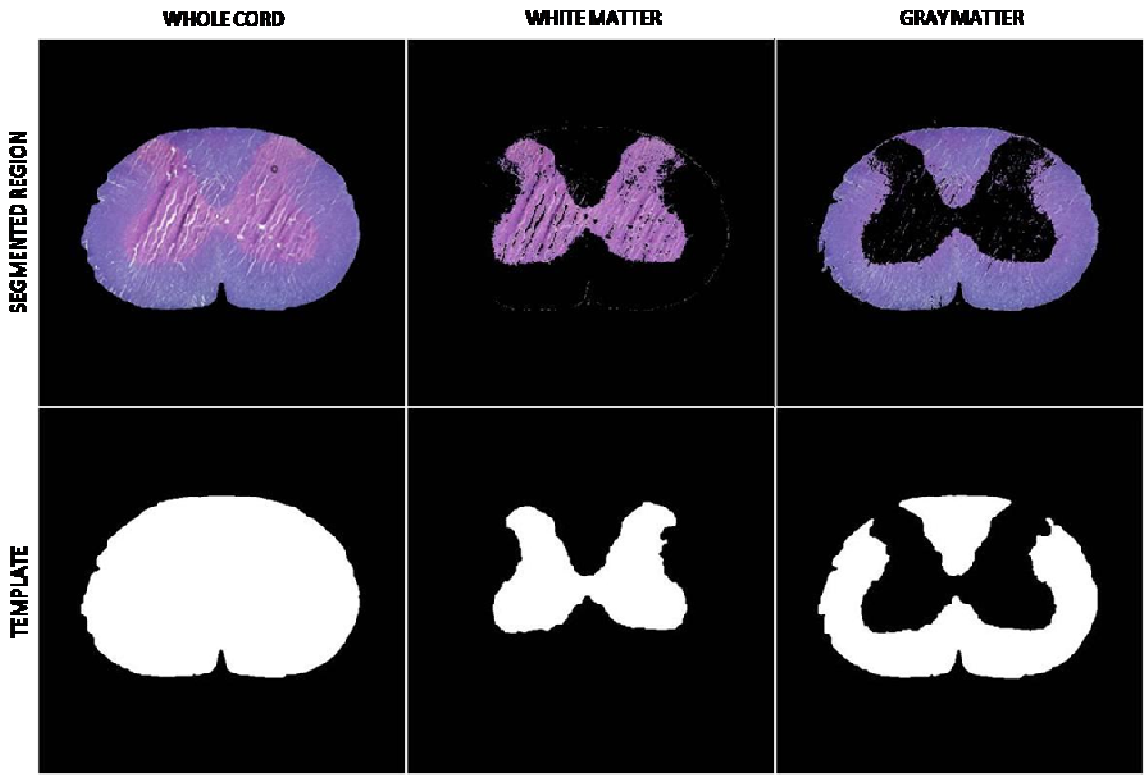

Figure 3.4: Templates formed based on segmented regions. Columns represent the regions of the cervical spinal cord. Rows show corresponding segmented images and templates formed based on the segmented images.

The L*a*b* histology image and the gray matter template were then used to form templates of the dorsal and ventral gray matter. The upper half of the L*a*b* histology image, containing the dorsal horn, was used to create the dorsal gray matter template while the lower half of the L*a*b* histology image, was used to create the ventral gray matter template. The L*a*b* histology image was modeled as concentric ellipses with their centers placed at the center of the image frame. The number of ellipses was fixed at 120 and they were equally spaced based upon the dorso-ventral and the dextro-sinister length of the whole cord. Pixel intensity was then sampled along the pixels lying on each ellipse. These intensity values were plotted as a function of the ellipse number and angle (theta) to form an angular intensity map. For the upper half of the L*a*b* histology

image, theta was calculated as the angle subtended at the center of the ellipse by the line joining a particular pixel lying on the ellipse and the pixel lying on the right end of the major axis of the ellipse. For the lower half of the L*a*b* histology image, theta was calculated as the angle subtended at the center of the ellipse by the line joining a particular pixel lying on the ellipse and the pixel lying on the left end of the major axis of the ellipse. Intensity analysis was then performed on the angular intensity map of the upper half of the L*a*b* histology image to obtain the angular and the elliptical bounds of the dorsal gray matter ROI. The bounds were then used to create a template of the dorsal gray matter. A similar analysis was performed on the angular intensity map of the lower half of L*a*b* histology image to obtain four angular and two elliptical bounds of the ventral gray matter ROIs. The bounds were then used to create a template of the ventral gray matter (*Figure 3.5*). These dorsal and ventral gray matter binary templates were in the same frame of reference as the white matter, gray matter and the whole cord template.

3.2.6.3 DTI segmentation and template formation

In order to identify the spinal cord in the DTI images, the MD image was used to separate the spinal cord from the agarose gelatin background. The MD was used because of the high contrast present between the spinal cord and the agarose gelatin in this DTI index. One single slice in the cervical section was selected from among the MD axial slices. This MD slice was first cropped to select a particular sample. Edge detection using the Canny method was then performed on the cropped ROI. The binary gradient mask created by edge detection was then dilated using image dilation in order to close

gaps in the outline of the whole cord. Once the gaps were closed, region filling was used to create the whole cord template. This was followed by image erosion in order to make the whole cord template smooth. This template was then used to segment the whole spinal cord in the FA, lADC and tADC images.

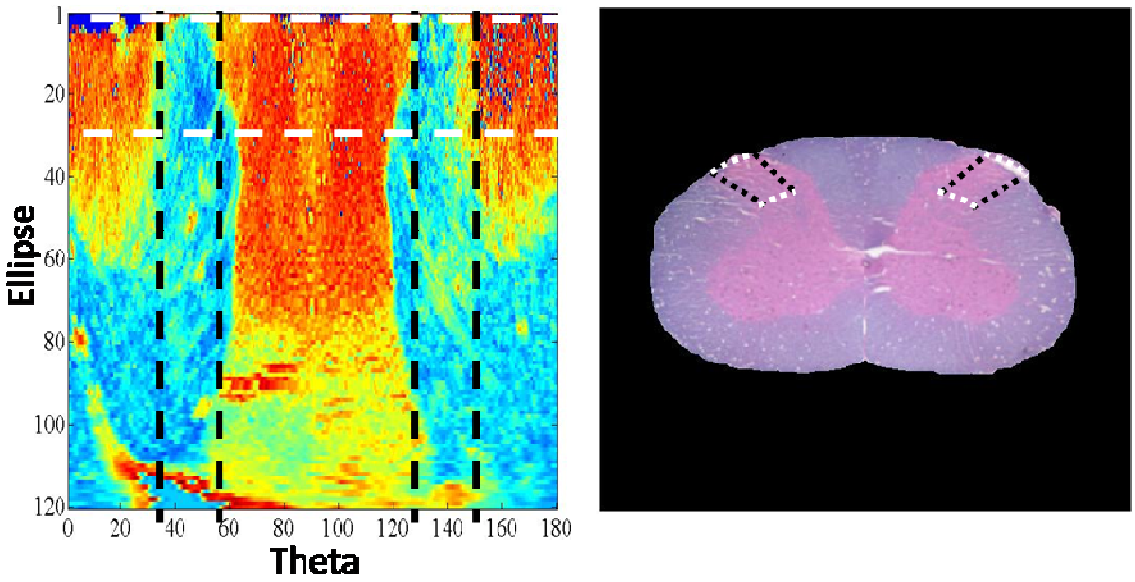

A

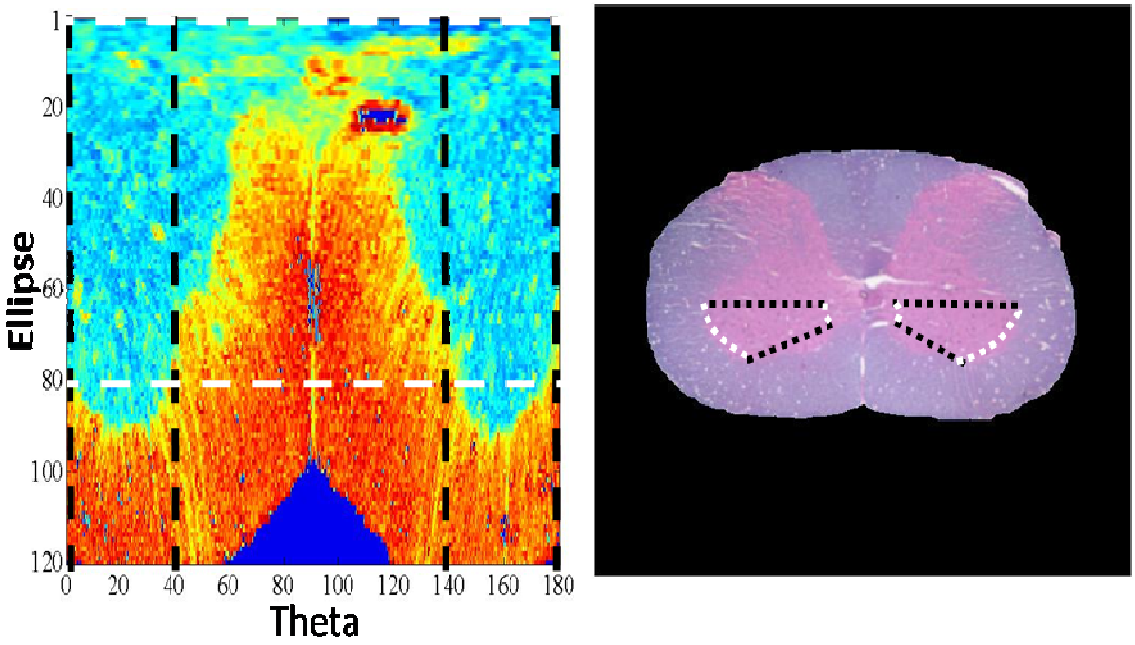

B

Figure 3.5: A) Angular intensity map and the dorsal template created from it. B) Angular intensity map and the ventral template created from it. Black dashed lines indicate the angular bounds while white dashed lines indicate elliptical bounds of the ROIs.

3.2.6.4 Registration

Once the histology and the DTI whole cord templates were created, they were used to register the DTI images to the histology images. The DTI whole cord template was first coarsely registered to the histology whole cord template using Matlab which was followed by a fine registration using a robust cost function implemented in FSL (Analysis Group, FMRIB, Oxford, UK).

To perform the coarse registration in Matlab, the histology whole cord template and the DTI whole cord template were first aligned to have the same frame of reference. The center of mass of each template was first found and aligned to center of the image frame. The center of mass coincided with the central canal in both the templates. Both the image frames were then zero padded to obtain a 1:1 aspect ratio. The angle of rotation of the DTI template image with respect to the histology template image was calculated using a Radon transformation (*Figure 3.6*). The scale factor in the x direction for scaling the DTI template image with respect to the histology template image was obtained from the ratio of the dextro-sinsiter length of the histology template to that of the DTI template. The scale factor in the y direction for scaling the DTI template image with respect to the histology template image was obtained from the ratio of the dorso-ventral length of the histology template to that of the DTI template. The angle of rotation and the scale factors in the x and the y direction were then used to create a 2-D affine transformation structure which was used to perform spatial transformation on the DTI template image using bilinear interpolation. In order to ensure the histology template

image and the DTI template image were in the same spatial coordinate system, the registered DTI template image was cropped and zero padded to achieve a 1:1 aspect ratio and the same image size as the histology template image while keeping the center of mass of the DTI template aligned to the center of the DTI template image frame.

To perform the fine registration, the histology template and the coarsely registered DTI template images were first converted into NIFTI data format using ImageJ and then read into FSL. The FLIRT module of FSL was then used to perform a rigid three degrees of freedom affine registration on the two templates using least square cost function. The reference histology template, the transformed DTI template and the registration parameters were then loaded back into Matlab for further analysis.

The same registration transformation then applied to the segmented FA, lADC and tADC images. The histology gray matter template was used to form gray matter diffusion maps for each sample in each group. The gray matter diffusion maps created from the C1 - C2 cervical slices of two of the subjects in the two weeks post injury group were excluded from creating the averaged visual diffusion maps but were included in the statistical analysis. This was because although they differed structurally from the slices obtained from the C4 - C5 levels, morphologically they had similar Rexed laminae as compared to the C4 - C5 cervical levels. The histology dorsal and ventral gray matter templates were used to segment the dorsal and the ventral gray matter ROIs in the DTI maps.

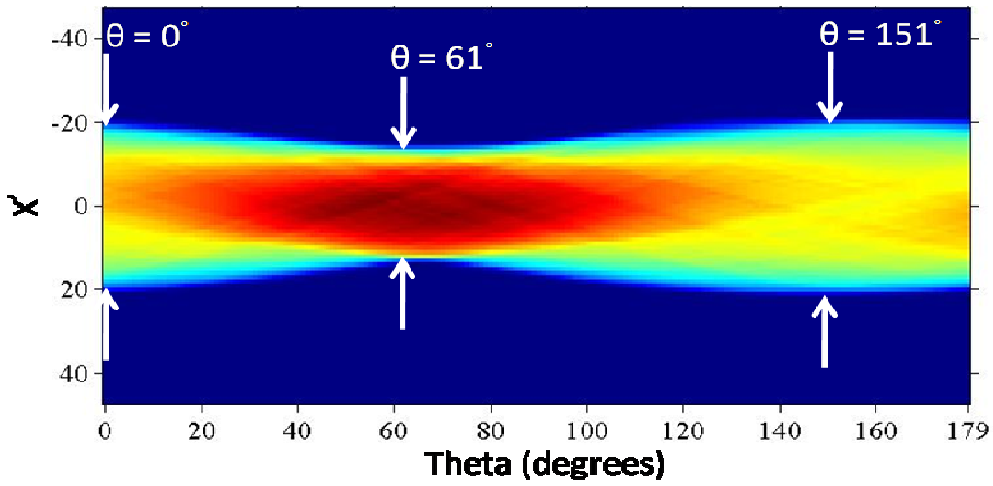

A

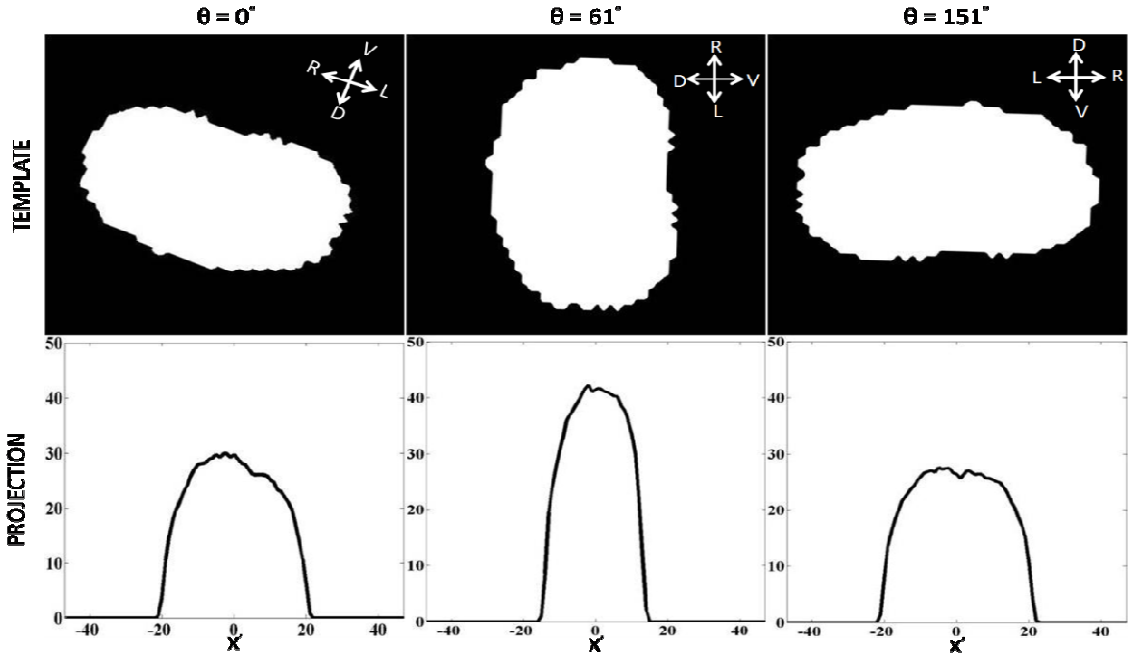

B

Figure 3.6: A) Radon transformation of the DTI whole cord template created from the MD image showing the projection of the DTI template along the radial line X' oriented at angle theta. B) Projections of the template along X' oriented at angles $\theta = 0^{\circ}$, $\theta = 61^{\circ}$ and $\theta = 151^{\circ}$.

3.2.7 Computing histological parameters

Once the ROIs were segmented, the toluidine blue stained histology images were used to calculate the size of the motoneurons in the ventral horns of the gray matter. Histological sections of the cervical spinal cord from the control group (n = 4), two weeks post injury (n = 4) and twenty five weeks post injury (n = 4) were used. Axial images were first captured at 4x magnification. These images were then used to determine the cytoarchitecture of the spinal cord based on Rexed laminae. The location of the lamina IX in the gray matter, which contains motoneurons, was determined based on the Rexed laminae for the cervical spinal cord (Paxinos 2004). These locations were then imaged at 40x magnification and the size of each motoneuron soma was measured manually. Only those motoneurons that were sliced through the center of the nucleus were measured and used for the subsequent statistical analysis

3.2.8 Statistical Analysis

All statistical analyses were carried out using SPSS Statistics 17 (SPSS Inc., Chicago, IL). FA, lADC and tADC values in the dorsal and the ventral gray matter ROIs were averaged across subjects in each group and then analyzed using an independent t-sample test. FA, lADC and tADC values in the gray matter were averaged across subjects in a group and then analyzed across recovery time points using a one-way analysis of variance. Tukey's post hoc test was used to compare the means. Motoneuron sizes were analyzed across recovery time points using a two level nested analysis of

variance. Recovery time was considered as the main group while subjects at each recovery time point was considered as a sub group. Games-Howell post hoc test was used to compare the means because of the unequal number of motoneurons sampled in each group. All tests were considered significant at $P<0.05$.

3.3 Results

3.3.1 Gray Matter Diffusivity Gradient

Individual diffusion maps showed a gradient in the diffusion values of the cervical spinal cord gray matter in controls as well as across recovery time points. The average diffusion maps were created by averaging the individual diffusion maps. In order to account for the difference in size of the gray matter across samples in each recovery time group, only pixels that were common to all the segmented gray matter templates of the samples in each recovery time group were considered. Note that this was performed only for visualization purposes. While considering the statistical significance of the changes in the diffusion values over time, the original gray matter template in each sample in each group was used. Average cervical spinal cord gray matter FA, lADC and tADC diffusion maps in control (n=5), two weeks post injury (n=3), fifteen weeks post injury (n=5) and twenty five weeks post injury (n=5) are shown in Figure 3.7.

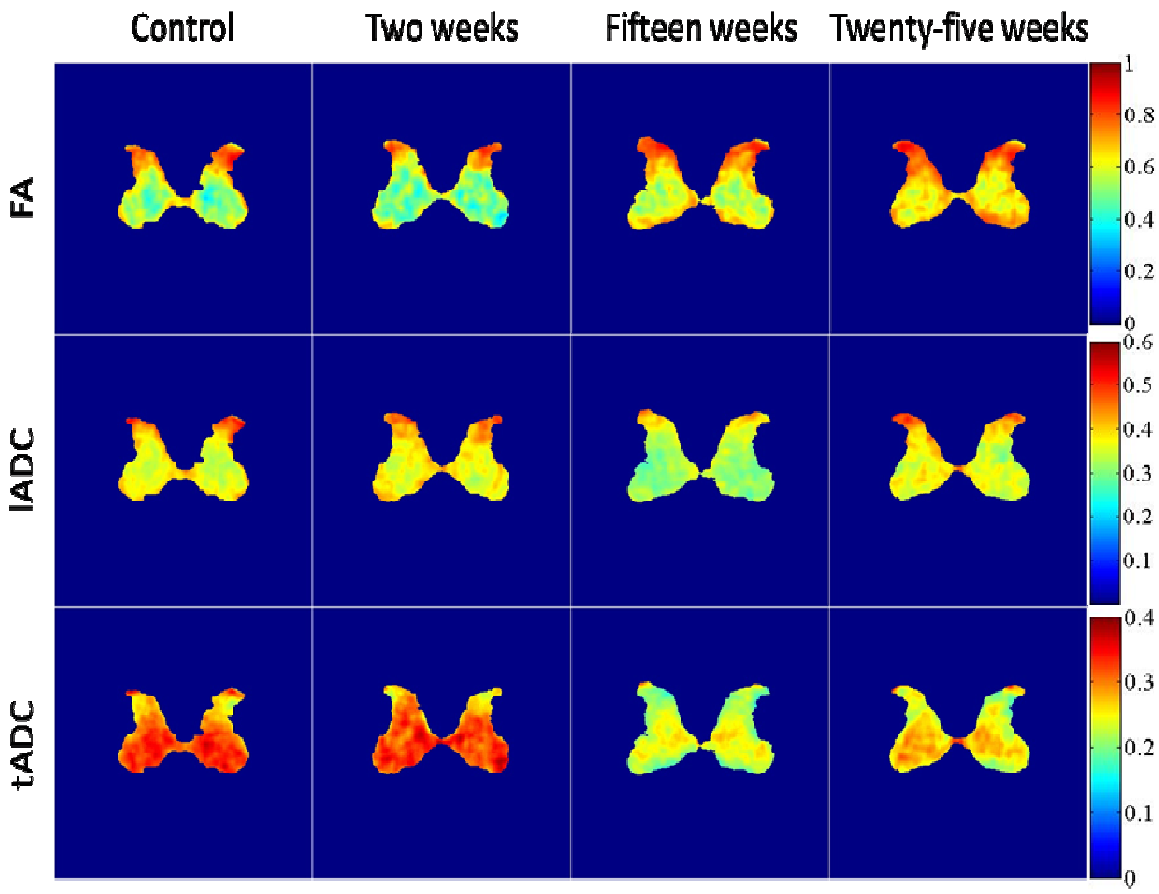

Figure 3.7: Ex vivo DTI images of the cervical spinal cord gray matter during recovery from contusion SCI. Columns represent cervical spinal cord gray matter at various recovery times and rows show corresponding fractional anisotropy (FA), longitudinal diffusion coefficient (lADC) and transverse diffusion coefficient (tADC) diffusion maps.

The diffusion maps showed an elevated fractional anisotropy in the dorsal horns as compared to the ventral horns in controls as well as at all recovery time points post injury. At twenty five weeks post injury, FA values in the whole gray matter showed an increase as compared to the FA values at two weeks and controls. Longitudinal apparent diffusion coefficient maps in the cervical gray matter show elevated lADC values in the dorsal horns of the gray matter as compared to the ventral horns in controls as well as at all recovery time points post injury. Transverse apparent diffusion coefficient maps in

the cervical gray matter showed elevated tADC values in the ventral horns of the gray matter as compared to the dorsal horns.

Analysis of the diffusion values in the dorsal and the ventral ROIs in the cervical gray matter in controls, fifteen weeks post injury and twenty five weeks post injury showed significant differences (*Figure 3.8A*). FA values in the dorsal ROI were significantly higher than in the ventral ROI in controls, fifteen weeks post injury and twenty five weeks post injury groups ($P < 0.05$). Similarly, lADC in the dorsal ROI was significantly higher than in the ventral ROI in controls, fifteen weeks post injury and twenty five weeks post injury groups ($P < 0.05$). Transverse apparent diffusion coefficient (tADC) showed a trend of higher values in the ventral ROI than the dorsal ROI, although the difference was not significant ($P = 0.497$ between control dorsal and ventral ROIs, $P = 0.365$ between two weeks post injury dorsal and ventral horns, $P = 0.672$ between fifteen weeks post injury dorsal and ventral horns, $P = 0.849$ between twenty five weeks post injury dorsal and ventral horns). *Figure 3.8B-C* shows regions of interest in the dorsal and ventral horns of the cervical gray matter respectively. The dorsal horn cytoarchitecture consisted largely of Rexed laminae I, II and III. Rexed laminae I and II showed the presence of thinly myelinated axons. The ventral horn cytoarchitecture consisted of Rexed laminae VII, VIII and IX and large neurons of Rexed laminae IX were defined as motoneurons.

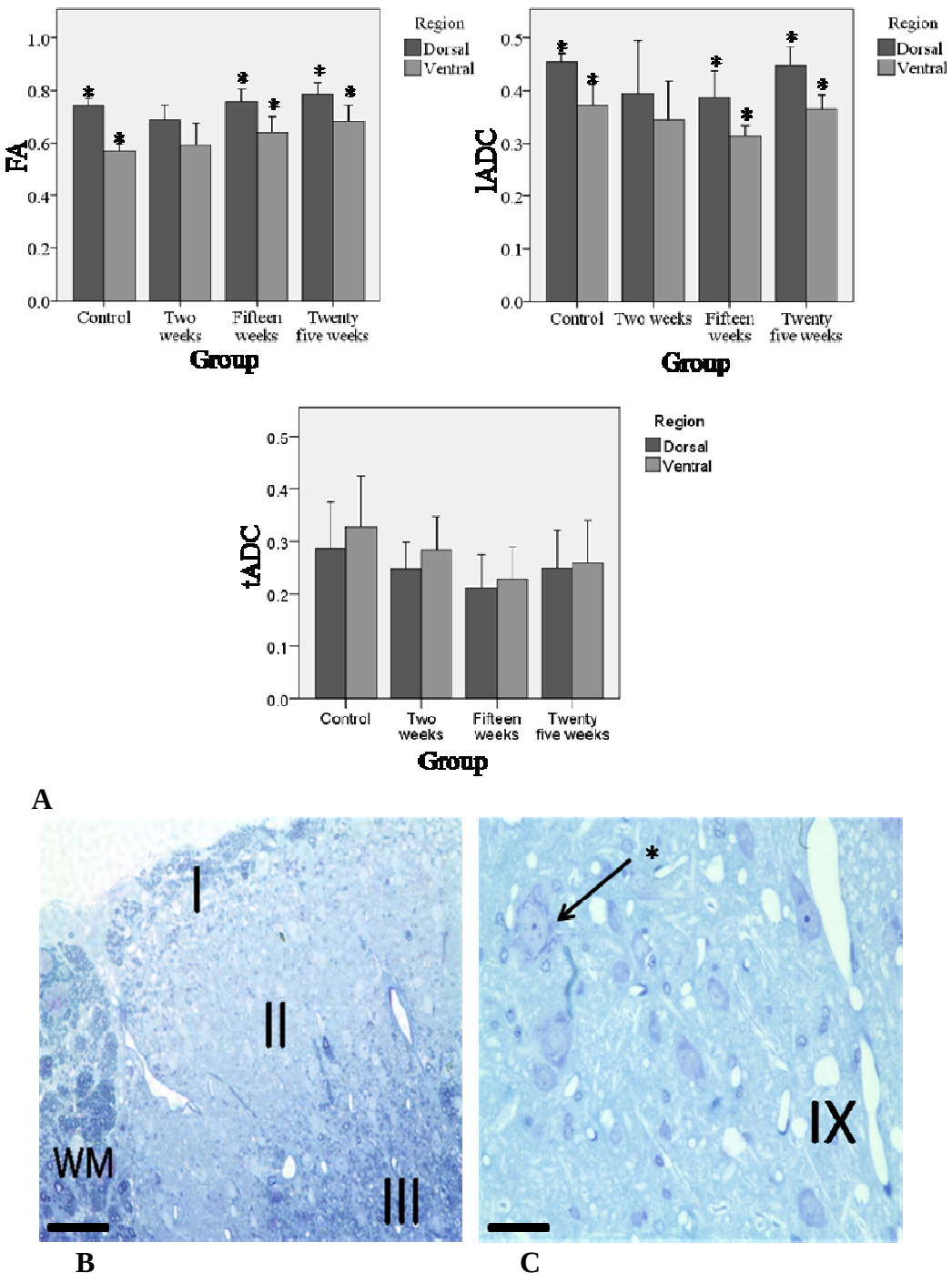

Figure 3.8: A) Ex vivo diffusion characteristics in dorsal and ventral regions of interest in the spinal cord gray matter. * = P < 0.05. Error bars = +1 SD. B) Rexed laminae I, II and III in the dorsal horn of the cervical spinal cord gray matter, WM = white matter. Scale bar = 50 µm. C) Rexed lamina IX in the ventral horn of the cervical spinal cord gray matter, * = motoneuron. Scale bar = 50 µm.

3.3.2 Overall Gray Matter Diffusivity

Group analysis of the diffusion values in the gray matter of the cervical spinal cord post injury showed significant changes (*Figure 3.9*). Fraction anisotropy (FA) values decreased at two weeks post injury as compared to controls. At fifteen weeks post injury, FA values were comparable to control FA values followed by an increase at twenty five weeks post injury as compared to controls. The FA value at twenty five weeks was significantly higher than the FA values at two week post injury ($P < 0.05$) and the FA values in controls ($P < 0.05$).

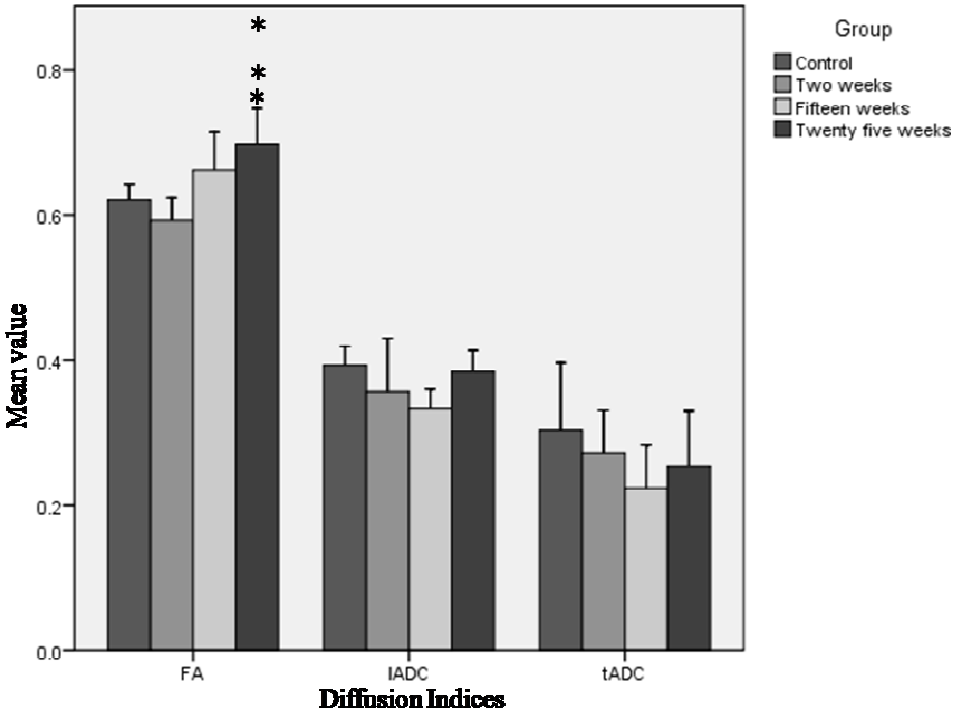

Figure 3.9: Ex vivo diffusion characteristics in the cervical spinal cord gray matter at recovery time points two weeks, fifteen weeks and twenty five weeks post injury. * = P < 0.05, compared to controls. ** = P < 0.05, compared to two weeks. Error bars = +1 SD.

3.3.3 Motoneuron Size

In order to verify that the changes in the cervical gray matter diffusion values reflected an underlying change in the neuronal structure of the gray matter, motoneuron sizes in the lamina IX of the ventral horns were obtained from the control group (n=4), two weeks post injury group (n=4) and twenty-five weeks post injury group (n=4). Group analysis of the size of the motor neurons showed a significant increase in the motoneuron size at two weeks ($P < 0.01$) and twenty five weeks ($P < 0.01$) post injury as compared to controls. The motoneurons also showed a significant increase in size at twenty five weeks post injury ($P < 0.01$) as compared to the motor neuron size at two weeks post injury (*Figure 3.10A*). At two weeks post injury the size of the motor neurons increased approximately by 9% from the size of the motoneurons in controls; whereas at twenty five weeks post injury, the size of the motoneurons increased by approximately 42% compared to controls. At twenty five weeks post injury there was an increase in the variability of the size of the motoneurons as compared to the variability in the motoneuron size among the control and two weeks post injury groups. Among the control and the two weeks post injury group, the two weeks post injury group had higher variability among the motoneuron sizes as seen in the histogram in *Figure 3.10b*.

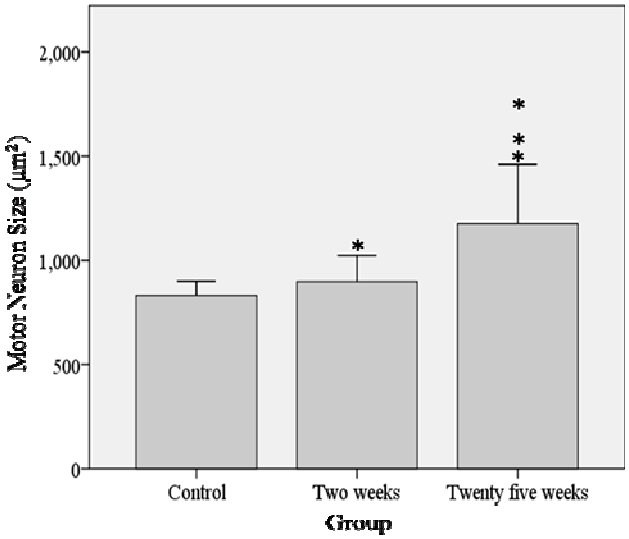

A

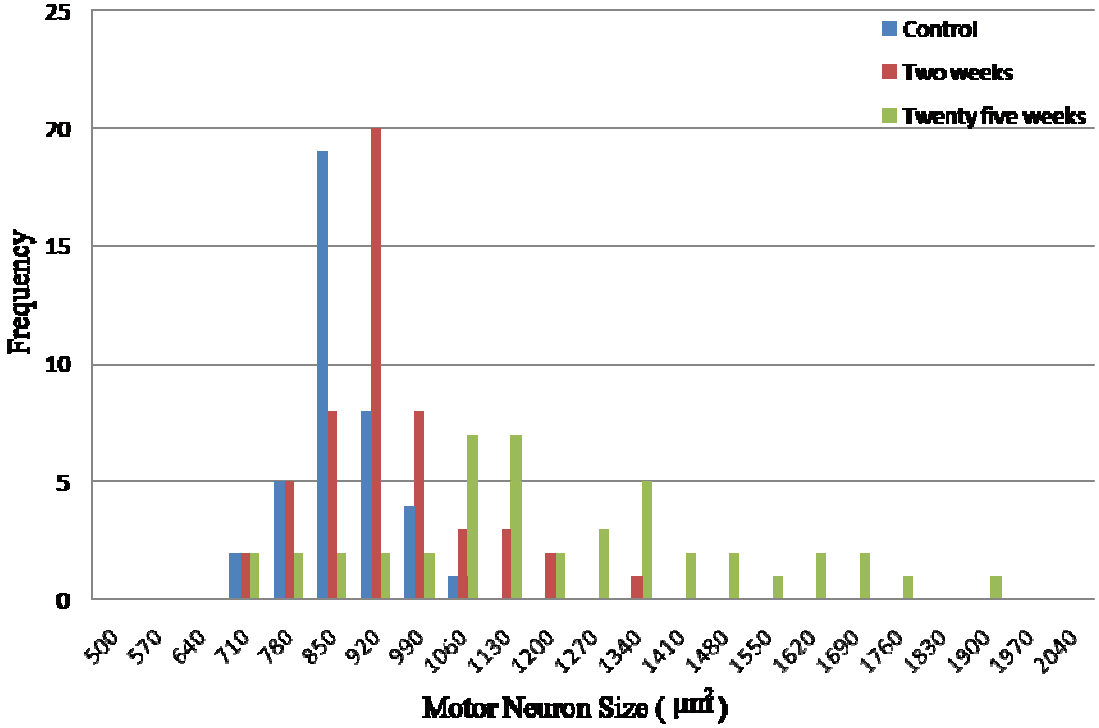

B

Figure 3.10: A) Motoneuron size in μm^2 in control, two weeks post injury and twenty five weeks post injury groups.* = P < 0.01, compared to control. ** = P < 0.01, compared to two weeks post injury. B) Histogram showing the variance in the size of the motor neurons (μm^2) among control, two weeks post injury and twenty five weeks post injury groups.

3.4 Discussion

3.4.1 Review of hypothesis and specific aims

The current study was motivated by the desire to quantify the diffusion properties using ex vivo DTI in the rat cervical spinal cord gray matter following a distal contusion spinal cord injury. We hypothesized that ex vivo DTI can detect changes in the diffusion characteristics in the rat cervical spinal cord gray matter remote from the lesion during long-term recovery from traumatic SCI. Further, we hypothesized that ex vivo diffusion characteristics in the dorsal horns of the rat cervical gray matter vary from the ex vivo diffusion characteristics in the ventral horns of the rat cervical gray matter and that DTI is sensitive to these variations. In order to test these hypotheses we developed an algorithm to automatically segment dorsal and ventral ROIs in the rat cervical gray matter based on histology templates and then use these ROIs to quantify the changes in the ex-vivo rat cervical DTI indices, temporally as well as spatially after a distal (T8) contusion spinal cord injury. Lastly, we hypothesized that ex vivo DTI values in the rat cervical spinal cord gray matter reflect the underlying microstructure of the spinal cord gray matter, specifically the structure of the neurons. In order to test this hypothesis we measured the size of the motoneurons in the cervical spinal cord gray matter remote during long term recovery from traumatic SCI.

3.4.2 Summary of results from the current study

To the best of our knowledge, the current investigation was the first to use ex vivo DTI to elucidate the spatial diffusion patterns in the rat cervical spinal cord gray matter following a distal contusion spinal cord injury. This study was also novel in the way it

used a robust automatic segmentation algorithm to segment ROIs in the rat cervical spinal cord gray matter. The segmentation technique, rather than being based on a histological atlas or user input, was based on the histology templates obtained from each specimen.

The diffusion parameters in the cervical spinal cord gray matter demonstrated a spatial variation. Fractional anisotropy (FA) values in the dorsal horn were significantly higher than the FA values in ventral horn in all groups. FA reflects underlying microstructural properties like myelin thickness, axon density and extracellular volume (Takahashi, Hackney et al. 2002; Mottershead, Schmierer et al. 2003; Gulani, Webb et al. 2001). Based on Rexed laminae, the ROI selected in the dorsal horns corresponded to laminae I, II and III. The ROI selected in the ventral horns corresponded to laminae VII, VIII and IX. Rexed laminae I, II and III showed the presence of thinly myelinated axons and high cellular density as compared to the Rexed laminae VII, VIII and IX. Rexed laminae VII, VIII and IX contained neurons and cellular support structure and did not contain axons (Steiner and Turner 1972; McClung and Castro 1978; Paxinos 2004). Thus, the higher FA in the dorsal horn as compared to the ventral horn could be explained by the presence of thinly myelinated axons in the dorsal horn. lADC values in the dorsal horn were significantly higher than the lADC values in all groups, except the 2 weeks post injury. Note that lADC reflects underlying microstructural properties such as myelin thickness, axon diameter along with neurofilament and microtubule density (Kinoshita, Ohnishi et al. 1999). The presence of thinly myelinated axons and the dense neurofilament and microtubules in the dorsal horn (Steiner and Turner 1972; McClung

and Castro 1978; Paxinos 2004) could explain the higher lADC values in the dorsal horn as compared to the ventral horns.

Diffusion parameters in the cervical spinal cord gray matter demonstrated changes over time post-injury. These changes included a decrease in diffusivity in the gray matter at two weeks post injury followed by a gradual recovery at twenty five weeks post injury. This trend in diffusivity was reflected in both lADC and tADC values. Our results support studies which report a similar decrease in the diffusivity values in the gray matter at the cervical level post SCI (Ellingson, Ulmer et al. 2006; Ellingson, Kurpad et al. 2008). Ellingson et al. reported a significant decrease in lADC and tADC values at two weeks, fifteen weeks post injury and twenty five weeks post injury as compared to controls. They also reported a decrease in FA values from two weeks through fifteen weeks post injury followed by a significant increase in FA at twenty five weeks post injury.

The observed decrease in the diffusion values in the cervical gray matter might be caused by a change in the ratio of intracellular to extracellular water volume due to cytotoxic edema (Haku, Miyasaka et al. 2006; Schwartz and Hackney 2003). An increased interstitial pressure could also lead to a prolonged hypoperfusion seen after injury (Tator and Koyanagi 1997; Haku, Miyasaka et al. 2006). This leads to an accumulation of water within the slow intracellular compartment further causing a decrease in the diffusion values at two weeks post injury (Stanisz, Webb et al. 2004). Studies have shown that diffusion in white matter is reduced in a model of cytotoxic edema (Ebisu, Naruse et al. 1993). An increase in intracellular water leads to a reduction in tADC and lADC due to an increase in restricted diffusion (Stanisz and Henkelman

2001). Stanisz et al. provided a model to fit the diffusion parameters and have used that model to predict the effects of axonal swelling on the diffusion characteristics in white matter. They found that the water shift from the extracellular compartment into the highly restricted intracellular compartment was the major cause of decreased diffusion (Stanisz, Szafer et al. 1997; Stanisz, Henkelman et al. 2001). At fifteen and twenty five weeks post injury, the decrease in the diffusion values can be explained by the increase in the cellular swelling due to chromatolysis. This is supported by histological evidence which shows an increase in the size of the soma of motor neurons as well as the dissolution of Nissl substance both of which are indicators of chromatolysis (Paxinos 2004).

Fractional anisotropy values in the whole cervical spinal cord gray matter decreased at two weeks followed by an increase to control levels at fifteen weeks. At twenty five weeks the FA values are significantly higher than controls and at two weeks post injury. These results support previous studies which report a similar trend in the FA values over time post SCI (Ellingson, Kurpad et al. 2008). To verify that the increase in FA values at twenty five weeks post injury reflected the chronic response following spinal cord injury, the size of the motoneurons in the ventral horns was measured. The size of the motor neuron in lamina IX showed changes which could explain the observed trend in FA values. At twenty five weeks, the size of the motoneurons increased significantly as compared to controls and two weeks. As the motoneurons increase in size, the extracellular volume is likely decreased. This could be the driving factor behind the decrease in diffusivity at twenty five weeks as compared to controls and two weeks post injury. Another factor that could contribute to the changes in the anisotropy is changes in the structure of dendrites post spinal cord injury. Studies have shown a

correlation between motoneuron soma size and dendritic features like dendritic length and branching (Ulfhake and Kellerth 1982; Kitzman 2005). Overall, histological evidence supports the notion that axotomized motoneurons in the cervical spinal cord gray matter are undergoing morphological changes which are consistent with cell swelling and chromatolysis following a distal contusion injury at the T8 level (McIlwain and Hoke 1999; McIlwain and Hoke 2005). We see similar changes in motor neurons in the ventral horn although these motor neurons are not axotomized. These changes could lead to a change in the ratio of the extracellular volume to the intracellular volume which could explain the increase in FA at chronic stages.

3.4.3 Clinical Implications

Performing DTI to map the diffusion characteristics in the gray matter may be beneficial as these diffusion properties can be correlated to the cytoarchitecture of the gray matter. Based on Rexed laminae, evaluation of the diffusion values in specific laminae can be correlated to functional characteristics. Changes in diffusion values in specific laminae over different recovery time points can then be used to predict functional recovery or deterioration.

Acquiring DTI at the lesion center during recovery from traumatic SCI can be difficult due to morphological changes in the spinal cord around the lesion center, and due to artifacts associated with metal surgical implants used to stabilize the injured spine. In order to overcome these difficulties, performing DTI on regions remote from the traumatic lesion could be beneficial in monitoring the state of the spinal cord during

recovery post SCI. Based on this study, gray matter in regions remote from the traumatic lesion are found to be sensitive to injury.

3.4.4 Study Limitations

In this current study, diffusion characteristics in the gray matter were only correlated to motor neuron sizes in the lamina IX of the cervical gray matter. Additional in depth quantitative analysis of the changes in the microstructural characteristics of the cellular structure in the gray matter is necessary in order determine the specific mechanisms behind the observed changes in the diffusion properties in the gray matter. Specifically, neuron density and changes in the neuronal structure in different laminae in the gray matter have to be established at different recovery time points post spinal cord injury.

The current study utilized DTI data obtained from the injured spinal cord gray matter in the secondary acute to the chronic stages of recovery. Primary acute (< 2 weeks post injury) were not explored in this study due to concerns with increased mortality. In order to determine the accurate temporal and spatial progression of changes in DTI values during primary acute stages, DTI needs to performed in specimens at recovery points less than two weeks.

In this current study, it was established that ex vivo DTI measurements in regions rostral to the injury site show changes which are specific and sensitive to the injury post a contusion spinal cord injury at the T8 level. However, in order to completely understand the mechanism of changes in diffusion characteristics in the gray matter throughout the

spinal cord gray matter, DTI values needs to be analyzed in the gray matter caudal to the injury site as well.

BIBLIOGRAPHY

Aoyama, T., K. Hida, et al. (2007). "Ultra-early MRI showing no abnormality in a fall victim presenting with tetraparesis." Spinal Cord **45**(10): 695-699.

Basser, P. J. and D. K. Jones (2002). "Diffusion-tensor MRI: theory, experimental design and data analysis - a technical review." NMR Biomed **15**(7-8): 456-467.

Beaulieu, C. (2002). "The basis of anisotropic water diffusion in the nervous system - a technical review." NMR Biomed **15**(7-8): 435-455.

Bloch, F., W. W. Hansen, et al. (1946). "Nuclear induction." Phys. Rev. **69**: 127.

Bose, P., R. Parmer, et al. (2005). "Morphological changes of the soleus motoneuron pool in chronic midthoracic contused rats." Exp Neurol **191**(1): 13-23.

Brown, R. (1828). "A brief account of microscopical observations made in the months of June, July and August, 1827, on the particles contained in the pollen of plants; and on the general existence of active molecules in organic and inorganic bodies." Phil Mag **4**: 161-173.

Budde, M. D., J. H. Kim, et al. (2007). "Toward accurate diagnosis of white matter pathology using diffusion tensor imaging." Magn Reson Med **57**(4): 688-695.

Budde, M. D., M. Xie, et al. (2009). "Axial diffusivity is the primary correlate of axonal injury in the experimental autoimmune encephalomyelitis spinal cord: a quantitative pixelwise analysis." J Neurosci **29**(9): 2805-2813.

Busch, S. A. and J. Silver (2007). "The role of extracellular matrix in CNS regeneration." Curr Opin Neurobiol **17**(1): 120-127.

Casha, S., W. R. Yu, et al. (2001). "Oligodendroglial apoptosis occurs along degenerating axons and is associated with FAS and p75 expression following spinal cord injury in the rat." Neuroscience **103**(1): 203-218.

Damadian, R. (1971). "Tumor detection by nuclear magnetic resonance." Science **171**: 1151-1153.

DeBoy, C. A., J. Zhang, et al. (2007). "High resolution diffusion tensor imaging of axonal damage in focal inflammatory and demyelinating lesions in rat spinal cord." Brain **130**(Pt 8): 2199-2210.

Deo, A. A., R. J. Grill, et al. (2006). "In vivo serial diffusion tensor imaging of experimental spinal cord injury." J Neurosci Res **83**(5): 801-810.

Dickinson, W. C. (1950). "Dependence of the 19F nuclear resonance position on chemical compound." Phys. Rev. **77**: 736.

Ditunno, J. F., J. W. Little, et al. (2004). "Spinal shock revisited: a four-phase model." Spinal Cord **42**(7): 383-395.

Ebisu, T., Naruse, S., et al. (1993). "Discrimination between different types of white matter edema with diffusion-weighted MR imaging." J. Magn. Reson. Imag. 3: 863–868.

Ehlers, M. D. (2004). "Deconstructing the axon: Wallerian degeneration and the ubiquitin-proteasome system." Trends Neurosci **27**(1): 3-6.

Einstein, A. (1905). "Uber die von der molekularkinetischen Theorie der Warme geforderte Bewegung von in ruhenden Flussigkeiten suspendierten Teilchen." Annalen der Physik **17**: 549-560.

Ellingson, B. M., S. N. Kurpad, et al. (2008). "In vivo diffusion tensor imaging of the rat spinal cord at 9.4T." J Magn Reson Imaging **27**(3): 634-642.

Ellingson, B. M., S. N. Kurpad, et al. (2008). "Ex vivo diffusion tensor imaging and quantitative tractography of the rat spinal cord during long-term recovery from moderate spinal contusion." J Magn Reson Imaging **28**(5): 1068-1079.

Ellingson, B. M., J. L. Ulmer, et al. (2008). "Diffusion tensor MR imaging in chronic spinal cord injury." AJNR Am J Neuroradiol **29**(10): 1976-1982.

Ellingson, B. M., J. L. Ulmer, et al. (2006). "Morphology and morphometry in chronic spinal cord injury assessed using diffusion tensor imaging and fuzzy logic." Conf Proc IEEE Eng Med Biol Soc **1**: 1885-1888.

Ellingson, B. M., J. L. Ulmer, et al. (2006). "A new technique for imaging the human spinal cord in vivo." Biomed Sci Instrum **42**: 255-260.

Ellingson, B. M., J. L. Ulmer, et al. (2008). "Morphology and morphometry of human chronic spinal cord injury using diffusion tensor imaging and fuzzy logic." Ann Biomed Eng **36**(2): 224-236.

Farber, J. L. (1990). "The role of calcium ions in toxic cell injury." Environ Health Perspect **84**: 107-111.

Faulkner, J. R., J. E. Herrmann, et al. (2004). "Reactive astrocytes protect tissue and preserve function after spinal cord injury." J Neurosci **24**(9): 2143-2155.

Fleming, J. C., M. D. Norenberg, et al. (2006). "The cellular inflammatory response in human spinal cords after injury." Brain **129**(Pt 12): 3249-3269.

Ford, J. C., D. B. Hackney, et al. (1994). "MRI characterization of diffusion coefficients in a rat spinal cord injury model." Magn Reson Med **31**(5): 488-494.

Gray, M. (1918). Gray's Anatomy of the Human Body. Philadelphia, Lea & Febiger.

Gulani, V., Webb, A.G., Duncan, I.D., Lauterbur, P.C. "Apparent diffusion tensor measurements in myelin-deficient rat spinal cords." Magn. Reson. Med. **45**: 191–195.

Haku, T., N. Miyasaka, et al. (2006). "Transient ADC change precedes persistent neuronal death in hypoxic-ischemic model in immature rats." Brain Res **1100**(1): 136-141.

Herrmann, J. E., T. Imura, et al. (2008). "STAT3 is a critical regulator of astrogliosis and scar formation after spinal cord injury." J Neurosci **28**(28): 7231-7243.

Hill, C. E., M. S. Beattie, et al. (2001). "Degeneration and sprouting of identified descending supraspinal axons after contusive spinal cord injury in the rat." Exp Neurol **171**(1): 153-169.

Hofling, A. A., J. H. Kim, et al. (2009). "Diffusion tensor imaging detects axonal injury and demyelination in the spinal cord and cranial nerves of a murine model of globoid cell leukodystrophy." NMR Biomed **22**(10): 1100-1106.

Huang, D. W., L. McKerracher, et al. (1999). "A therapeutic vaccine approach to stimulate axon regeneration in the adult mammalian spinal cord." Neuron **24**(3): 639-647.

Jenkinson, M. and S. Smith (2001). "A global optimisation method for robust affine registration of brain images." Med Image Anal **5**(2): 143-156.

Kakulas, B. A. (2004). "Neuropathology: the foundation for new treatments in spinal cord injury." Spinal Cord **42**(10): 549-563.

Kandel, E. R., J. H. Schwartz, et al. (2000). Principles of neural science. New York, McGraw-Hill, Health Professions Division.

Kim, J. H., M. D. Budde, et al. (2006). "Detecting axon damage in spinal cord from a mouse model of multiple sclerosis." Neurobiol Dis **21**(3): 626-632.

Kim, J. H., J. Haldar, et al. (2009). "Diffusion tensor imaging of mouse brain stem and cervical spinal cord." J Neurosci Methods **176**(2): 186-191.

Kim, J. H., D. N. Loy, et al. "Diffusion tensor imaging at 3 hours after traumatic spinal cord injury predicts long-term locomotor recovery." J Neurotrauma **27**(3): 587-598.

Kinoshita, Y., Ohnishi, et al. (1999). "Apparent diffusion coefficient on rat brain and nerves intoxicated with methylmercury." Environ Res. **80**(4):348-54.

Kitzman, P. (2005). "Alteration in axial motoneuronal morphology in the spinal cord injured spastic rat." Exp Neurol **192**(1): 100-108.

Kozlowski, P., D. Raj, et al. (2008). "Characterizing white matter damage in rat spinal cord with quantitative MRI and histology." J Neurotrauma **25**(6): 653-676.

Lauterbur, P. C. (1973). "Image formation by induced local interactions: examples employing nuclear magnetic resonance." Nature **242**: 190-191.

Le Bihan, D., E. Breton, et al. (1986). "MR imaging of intravoxel incoherent motions: application to diffusion and perfusion in neurologic disorders." Radiology **161**(2): 401-407.

Lemieux, L., N. D. Kitchen, et al. (1994). "Voxel-based localization in frame-based and frameless stereotaxy and its accuracy." Med Phys **21**(8): 1301-1310.

Lu, J., K. W. Ashwell, et al. (2000). "Advances in secondary spinal cord injury: role of apoptosis." Spine (Phila Pa 1976) **25**(14): 1859-1866.

Madi, S., K. M. Hasan, et al. (2005). "Diffusion tensor imaging of in vivo and excised rat spinal cord at 7 T with an icosahedral encoding scheme." Magn Reson Med **53**(1): 118-125.

Mansfield, P. (1977). " Multiplanar image formation using NMR spin echoes." J. Phys. C: Solid State Phys. **10**: L55-L58.

McClung, J. R., Castro, A. J. (1978). "Rexed's laminar scheme as it applies to the rat cervical spinal cord." Exp Neurol. **1;58**(1):145-148.

McIlwain, D. L. and V. B. Hoke (1999). "Magnitude, laterality, and uniformity of swelling in axotomized spinal motoneurons: lack of evidence for influence by the distal stump." Exp Neurol **157**(1): 161-168.

McIlwain, D. L. and V. B. Hoke (2005). "The role of the cytoskeleton in cell body enlargement, increased nuclear eccentricity and chromatolysis in axotomized spinal motor neurons." BMC Neurosci **6**: 19.

Merrill, J.E., Zimmerman, R.P., 1991. Natural and induced cytotoxicity of oligodendrocytes by microglia is inhibitable by TGFβ. GLIA 4, 327–331

Moseley, M. E., J. Kucharczyk, et al. (1991). "Anisotropy in diffusion-weighted MRI." Magn Reson Med **19**(2): 321-326.

Moseley, M. E., J. Kucharczyk, et al. (1990). "Diffusion-weighted MR imaging of acute stroke: correlation with T2-weighted and magnetic susceptibility-enhanced MR imaging in cats." AJNR Am J Neuroradiol **11**(3): 423-429.

Mottershead, J.P., Schmierer, K., et al. (2003) "High field MRI correlates of myelin content and axonal density in multiple sclerosis - a post-mortem study of the spinal cord." J Neurol. 250(11):1293–301.

Narayana, P., R. Abbe, et al. (1999). "Does loss of gray- and white-matter contrast in injured spinal cord signify secondary injury? In vivo longitudinal MRI studies." Magn Reson Med **41**(2): 315-320.

Nimmerjahn, A., F. Kirchhoff, et al. (2005). "Resting microglial cells are highly dynamic surveillants of brain parenchyma in vivo." Science **308**(5726): 1314-1318.

Norenberg, M. D., J. Smith, et al. (2004). "The pathology of human spinal cord injury: defining the problems." J Neurotrauma **21**(4): 429-440.

Park, E., A. A. Velumian, et al. (2004). "The role of excitotoxicity in secondary mechanisms of spinal cord injury: a review with an emphasis on the implications for white matter degeneration." J Neurotrauma **21**(6): 754-774.

Paxinos, G. (2004). The rat nervous system. Amsterdam ; Boston, Elsevier Academic Press.

Paxinos, G. and J. K. Mai (2004). The human nervous system. Amsterdam ; Boston, Elsevier Academic Press.

Pierpaoli, C. and P. J. Basser (1996). "Toward a quantitative assessment of diffusion anisotropy." Magn Reson Med **36**(6): 893-906.

Pineau, I. and S. Lacroix (2007). "Proinflammatory cytokine synthesis in the injured mouse spinal cord: multiphasic expression pattern and identification of the cell types involved." J Comp Neurol **500**(2): 267-285.

Povlishock, J. T. (1993). "Pathobiology of traumatically induced axonal injury in animals and man." Ann Emerg Med **22**(6): 980-986.

Proctor, W. G. and F. C. Yu (1950). "The dependence of a nuclear magnetic resonance frequency upon chemical compound." Phys. Rev. **77**: 717.

Purcell, E. M., H. C. Torrey, et al. (1946). "Resonance absorption by nuclear magnetic moments in a solid." Phys. Rev. **69**: 37-38.

Rexed, B. (1954). "A cytoarchitectonic atlas of the spinal cord in the cat." J Comp Neurol **100**(2): 297-379.

Sagiuchi, T., S. Tachibana, et al. (2002). "Diffusion-weighted MRI of the cervical cord in acute spinal cord injury with type II odontoid fracture." J Comput Assist Tomogr **26**(4): 654-656.

Sakamoto, A., S. T. Ohnishi, et al. (1991). "Relationship between free radical production and lipid peroxidation during ischemia-reperfusion injury in the rat brain." Brain Res **554**(1-2): 186-192.

Schnell, L., S. Fearn, et al. (1999). "Cytokine-induced acute inflammation in the brain and spinal cord." J Neuropathol Exp Neurol **58**(3): 245-254.

Schwartz , E.D. and Hackney, D.B. (2003). "Diffusion-weighted MRI and the evaluation of spinal cord axonal integrity following injury and treatment." Exp Neurol 184(2):570-589.

Schwartz, E. D., E. T. Cooper, et al. (2005). "MRI diffusion coefficients in spinal cord correlate with axon morphometry." Neuroreport **16**(1): 73-76.

Schwartz, E. D., J. Duda, et al. (2005). "Spinal cord diffusion tensor imaging and fiber tracking can identify white matter tract disruption and glial scar orientation following lateral funiculotomy." J Neurotrauma **22**(12): 1388-1398.

Shi, R. and J. D. Pryor (2002). "Pathological changes of isolated spinal cord axons in response to mechanical stretch." Neuroscience **110**(4): 765-777.

Sidman, R. L., J. B. Angevine, et al. (1971). Atlas of the mouse brain and spinal cord. Cambridge, Mass.,, Harvard University Press.

Smith, C., M. Berry, et al. (2001). "Differential expression of fibroblast growth factor-2 and fibroblast growth factor receptor 1 in a scarring and nonscarring model of CNS injury in the rat." Eur J Neurosci **13**(3): 443-456.

Song, S. K., S. W. Sun, et al. (2003). "Diffusion tensor imaging detects and differentiates axon and myelin degeneration in mouse optic nerve after retinal ischemia." Neuroimage **20**(3): 1714-1722.

Song, S. K., S. W. Sun, et al. (2002). "Dysmyelination revealed through MRI as increased radial (but unchanged axial) diffusion of water." Neuroimage **17**(3): 1429-1436.

Song, S. K., J. Yoshino, et al. (2005). "Demyelination increases radial diffusivity in corpus callosum of mouse brain." Neuroimage **26**(1): 132-140.

Stanisz, G.J., Szafer, A., et al. (1997). "An analytical model of restricted diffusion in bovine optic nerve." Magn. Reson. Med. 37: 103–111.

Stanisz, G., Henkelman, R.M. (2001). "Effects of cellular swelling on diffusion in white matter." In Proceedings of the 9th ISMRM, Glasgow, Scotland, 2001; 350.

Stanisz, G. J., S. Webb, et al. (2004). "MR properties of excised neural tissue following experimentally induced inflammation." Magn Reson Med **51**(3): 473-479.

Steiner, T. J., Turner L.M. (1972). "Cytoarchitecture of the rat spinal cord." J Physiol. 222(2):123-125.

Takahashi, M., Hackney, D.B., et al. (2002). "Magnetic resonance microimaging of intraaxonal water diffusion in live excised lamprey spinal cord." Proc Natl Acad Sci U S A. 10;99(25):16192-6.

Tator, C. H. and I. Koyanagi (1997). "Vascular mechanisms in the pathophysiology of human spinal cord injury." J Neurosurg **86**(3): 483-492.

Tu, T. W., J. H. Kim, et al. (2010). "Full tensor diffusion imaging is not required to assess the white-matter integrity in mouse contusion spinal cord injury." J Neurotrauma **27**(1): 253-262.

Ulfhake, B., Kellerth, J.O., (1982). "Does alpha-motoneurone size correlate with motor unit type in cat tricep surae?" Brain Res. **251**, 201–209.

Waxman, S. G. (1989). "Demyelination in spinal cord injury." J Neurol Sci **91**(1-2): 1-14.

Wrathall, J. R., Y. D. Teng, et al. (1996). "Amelioration of functional deficits from spinal cord trauma with systemically administered NBQX, an antagonist of non-N-methyl-D-aspartate receptors." Exp Neurol **137**(1): 119-126.

Zhang, J., M. Jones, et al. (2009). "Diffusion tensor magnetic resonance imaging of Wallerian degeneration in rat spinal cord after dorsal root axotomy." J Neurosci **29**(10): 3160-3171.